

1 Experimental study of debris transport driven by a tsunami-like wave: Application
2 for non-uniform density groups and obstacles
3

4
5 Hyoungsu Park^{*1}, Myung-Jin Koh², Daniel T. Cox³, Mohammad Shafiqul Alam⁴ and Sungwon Shin⁵
6

7 **Abstract**
8

9 Water-borne disaster debris can exacerbate the damage on the built-environment through debris impact and
10 debris damming loads and by decreasing the functionality of infrastructure systems after these events.
11 Therefore, an understanding of disaster debris transport is essential for disaster management. In this paper,
12 an experimental study of tsunami-driven debris spreading over a flat testbed was conducted considering
13 different density conditions of debris elements. Debris elements of two different materials (densities) were
14 considered various debris groups and starting orientation. The final dislocations and local velocity of debris
15 elements were measured optically and compared to flow velocity. Among two debris elements in a debris
16 group, it was found that debris elements of higher density affected the mean longitudinal displacement of
17 the less dense debris, but the less dense debris did not affect the displacement of higher density debris. Also,
18 it was found that the initial orientations of the debris groups had no measurable impact on the final
19 displacement. The effects of obstacles on the passage of debris and the probability of collision to obstacles
20 were examined and the process of debris-debris and debris-obstacle interactions from debris entrainment to
21 final dislocation was studied. It was found that the less dense debris had a higher probability of collision
22 with the obstacles compared to the more dense debris case. However, when the debris types were mixed,
23 the less dense debris had a lower probability of collision. Finally, the characteristics of debris dislocation
24 and velocity fields under various density conditions as a group were also evaluated. The reflected wave and
25 interaction among different debris play a role in the probability of collision. However, the density of each
26 debris element was a dominant factor in determining the collision probability.

27
28 **Keywords:** Debris transport, Density, Dislocation, Obstacle, Tsunami

¹ Assistant Professor, Department of Civil and Environmental Engineering, University of Hawai'i at Manoa, Honolulu, HI 96822, United States., *Corresponding Author (Hpark9@hawaii.edu).

² Graduate Student, Department of Civil and Environmental Engineering, University of Hawai'i at Manoa, Honolulu, HI, 96822, United States.

³ Professor, School of Civil and Construction Engineering, Oregon State University, Corvallis, OR, 97331, United States.

⁴ Postdoctoral Scholar, School of Civil and Construction Engineering, Oregon State University, Corvallis, OR, 97331, United States

⁵ Associate Professor, Department of Marine Science and Convergence Engineering Hanyang University, Ansan, Kyunggi-do, Republic of Korea.

29 **1. Introduction**

30

31 Extreme coastal events like hurricanes and tsunamis often generate and transport debris resulting in severe
32 damage to civil infrastructure systems (e.g., Chock et al., 2013; Naito et al., 2014;) and often adversely
33 affecting the resilience and recovery process of communities (Çelik et al., 2015). In particular, water-borne
34 debris such as shipping containers, vehicles, and wood logs are well known to exacerbate the structural
35 damage on the built environment through the debris impact (collision) and damming loads (e.g., Riggs et
36 al., 2014; Yeh et al., 2014). Moreover, debris transported over the land often decreases the functionality of
37 critical facilities and block access for initial rescue and recovery. It is also reported that the hurricane-driven
38 coastal debris removal could account for approximately 27% of the total disaster recovery cost in the USA
39 (FEMA, 2007). Therefore, a better understanding of water-driven debris transport is essential to predict
40 damages and losses on coastal communities and to develop a mitigation plan to minimize those losses and
41 improve the resilience against future extreme coastal events.

42 Over the years, our understanding of tsunami disaster debris has enriched from field reconnaissance,
43 numerical simulations, and laboratory experiments. Several field surveys reported marine debris transport
44 in the open ocean originating from tsunami runup and drawdown on land which is relevant for pollution
45 (e.g., Martinez et al., 2009; Murray et al., 2018) and changes in marine ecology (e.g., Miller et al., 2017) as
46 well as marine debris transport close to shore in navigable waterways and overland. A few debris studies
47 debris carried overland such as large boulders and sediment deposits to determine, for example, the intensity
48 of past tsunami events (e.g., Bourgeois and MacInnes, 2010; Paris et al., 2010, Etienne et al., 2011). For the
49 built environment, there are relatively few documented studies of debris transport overland. Naito et al.
50 (2014) performed the first field survey to evaluate the overall transport of debris from the 2011 Tohoku
51 Tsunami. They tracked the final dislocation of large debris such as shipping containers and vessels, then
52 estimated the angle of debris distribution from the origin, which is the spreading angle with a limit distance
53 (areas) based on the quantity at the origin. This approach is adopted in the current ASCE7/SEI 7-16 in
54 Chapter 6 (ASCE, 2017) to evaluate the debris hazard region under potential tsunami debris impact loading
55 if the region has relevant sources of debris such as vessel, shipping container, logs, and boulder.

56 There have been several numerical investigations for the aforementioned observed tsunami debris
57 phenomena, particularly boulder transport (e.g., Imamura et al., 2008) and sediment transport (Sugawara et
58 al., 2014) to aid in the understanding of tsunami hazards. However, there are relatively fewer studies of
59 tsunami debris transport in the engineering context, for example, the transport of construction debris from
60 damaged buildings and other components of the built environment. In their review of tsunami debris
61 transport and loads, Nistor et al., 2017a cites several numerical studies but had focused primarily on

62 modeling a single or relatively few debris elements leading to impact on structures. More recently, Park
63 and Cox (2019) showed how a Lagrangian tracking method with ad-hoc assumptions for the initiation and
64 grounding of debris can be used to advect debris at a community-wide scale. Kihara and Kaida (2020) used
65 a debris tracking model to assess the probability of debris striking an object. They compared their work to
66 laboratory simulations and considered two important aspects: the effects of reflected waves from structures
67 on the debris as it approaches the structure, and the diffusion of debris as it is transported. For the latter,
68 they added a numerical diffusion to recreate the conditions observed in the laboratory.

69 Subsequent to the 2011 Tohoku tsunami, there have been a number of tsunami debris studies based on
70 scaled hydraulic experiments (e.g., Riggs et al., 2014; Aghl et al., 2015; Xia et al., 2014; Ko et al, 2015;
71 Stolle et al., 2017; Stolle et al., 2018a, Shekhar et al., 2020). Most of these studies have mainly focused on
72 debris-structures impact or damming loads using varied shapes (e.g., shipping container, vehicles, box, and
73 pole) and materials (e.g., Wood, and Polyethylene). However, there have been relatively fewer experimental
74 studies that focused on tsunami driven debris motions and transportation including debris entrainment and
75 spreading. Yao et al. (2014) conducted a study of debris transport over a sloped bed with tsunami-like flow
76 conditions, evaluating the final dislocation of debris and compared that to the maximum flow inundation.
77 Rueben et al., (2015) examined the effect of multiple debris and fixed obstacles on debris motion, tracking
78 both individual debris elements as well as the center of mass of the group. Shafiei et al. (2016) developed
79 an equation for the debris speed under dam-break flow conditions as a function of the leading-edge velocity
80 of flow, mass, and projected area of single debris using an implemented accelerometer in debris. Goseberg
81 et al. (2016) reported a significant effect of the presence of obstacles on the moving distance of debris
82 utilizing Bluetooth Low Energy wireless connection to track the debris motion. Nistor et al. (2017b)
83 conducted a physical modeling study and determined the debris spreading angle, suggesting that the
84 spreading angle increases with the number of debris likely due to the debris interaction. Stolle et al. (2018b)
85 and Stolle et al. (2020) used a statistical approach considering debris speed and motions combined with
86 non-dimensional parameters to predict the probability of debris transport, analogous to approaches in wind
87 engineering (Tachikawa, 1983; Lin and Vanmarcke, 2008). The dependency of initial positions of two
88 debris including gap-ratio and lateral displacement is measured focusing on debris' rotation as well as
89 longitudinal and lateral displacement (von Hafen et al., 2021). Table 1 summarizes detailed information of
90 recent tsunami-driven debris transport experiments. However, most of the tsunami-driven debris transport
91 studies to date relied on relatively a small number of debris and debris configurations and they were still
92 limited to in representing the complicated multi-debris transport process including its generation,
93 entrainment, interactions with obstacles, spreading, and grounding.

94 TABLE 1 The summary of experimental research on tsunami-driven debris transportation.

95

Tracking Method	Shape	Debris			Material (Specific Gravity)	Interaction w/ Obstacles	Wave Type
		Dimension (cm) H × W × L	Number				
Yao et al. (2014)	Optical	Square Box	0.5×0.5×1.0	10, 20, 30	Polyethylene SG = 0.92	No	Solitary wave
Rueben et al. (2015)	Optical	Square Box	40×60×60	1, 4, 9	Plywood SG = 0.71	Yes	Tsunami like wave
Shafiei et al.(2016)	Optical, Sensor	Disc	(D)20×5	1	Acrylic + add mass SG=0.32, 0.46, 0.58	Yes	Dam break wave
Goseberg (2016)	*Smart debris	Shipping Container	6×6×15	3, 6	Polyethylene (w/sensor) SG = 0.92	Yes	Tsunami like wave
Nistor et al. (2017)	*Smart debris, Optical	Shipping Container	6×6×15	1, 3, 9, 18	Polyethylene (w/sensor) SG = 0.92	No	Tsunami like wave
Stolle et al. (2020);	Optical	Shipping Container	6×6×15	1, 3, 6, 2, 6, 12	Polyethylene SG = 0.418	Yes	Dam break wave
Current study	Optical	Square Box	5×10×10	20	Wood (SG = 0.65), HDPE (SG = 0.99)	Yes	Tsunami like wave

96 * Smart debris indicates the debris utilized the wireless sensor inside of debris for tracking. (Goseberg et al., 2016)

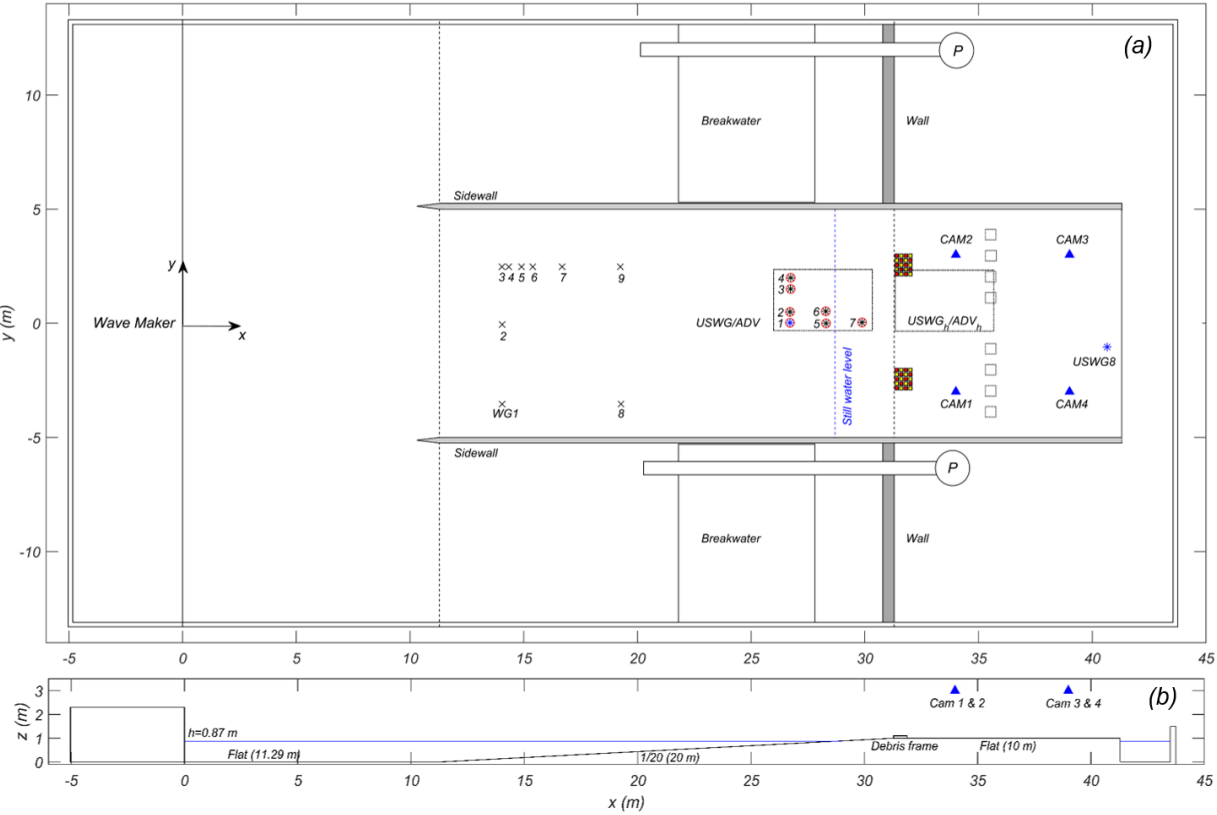
97 In this study, we performed an experimental study of multi-debris transport using grouped debris, which
 98 comprises of two types of debris with different density. We utilized optical measurement and observed the
 99 details on the debris entrainment, debris floating, and dragging under the various initial debris setups under
 100 a tsunami-like wave condition. The major objectives of this study include: 1) A better understanding of the
 101 overall process of multi-debris transport and its characteristics. 2) Evaluating the effects of varied density
 102 of grouped multi-debris in the debris transport. 3) Evaluating the effects of downstream obstacles to debris
 103 transport. These objectives are achieved in the following sections. Section 2 introduces the experiment
 104 setup and Section 3 provides the optical measurement process and preliminary results. Section 4 shows the
 105 results of debris advection including final debris moving distance, spreading angle, probability of collision
 106 to obstacles, and debris flow fields under varied grouped debris conditions. Section 5 discusses the
 107 limitations of current work, and Section 6 summarized the general findings in this study and suggested
 108 possible future works.

109 **2. Experimental setup**

110

111 The physical experiments were performed in the Directional Wave Basin at Oregon State University (Fig. 1). The wave basin was 48.8 m long (x -direction), 26.5 m wide (y -direction), and 2.1 m deep (z -direction),
 112 and was equipped with a segmented piston-type wavemaker with a maximum full stroke of 2.1 m and
 113 maximum velocity of 2.0 m/s. For the debris experiment, the uniform sloped and elevated bathymetry,
 114 installed in the middle of the basin (Fig. 1) were utilized. The profile of bathymetry consisted of an 11.29
 115 m flat section starting from the wavemaker ($x = 0$ m), 1:20 slope extended from $x = 11.29$ m to $x = 31.29$
 116 m, and a 10 m flat section, elevated 1.0 m above the basin floor and extending to $x = 41.29$ m. The total
 117 width of the slope and the elevated area was 10 m ($y = -5$ m to 5 m), and two brick walls (top and bottom)
 118 were installed as sidewalls at the sloped and flat sections. The bathymetry was capped with smooth concrete.
 119 Two multi-grouped debris sources (red and yellow checkerboard in Fig. 1a) were located at the start of the
 120 flat section ($x = 31.29$ m). Sidewalls ran parallel to the x -axis on either side, and the end of the flat section
 121 was open to the surrounding water such that the inundating water could flow unimpeded over the back of
 122 the test section. This is the same general set-up used for other overland flow experiments (e.g., Tomizek et
 123 al. 2020, Duncan et al., submitted).

125



126

127 **Figure 1:** Sketch of the experimental setup: (a) plan and (b) profile view. At Fig. 1a, each symbol of ‘ \times ’
 128 and ‘*’ indicates the wire resistance wave gage (WG) and ultra-sonic wave gage (USWG), while ‘ \circ ’
 129 indicates the location of acoustic-Doppler Velocimeter (ADV), which are overlapped to USWG locations.
 130 Triangle indicates the location of four cameras. In Fig. 1b, the debris frame indicates the location of the
 131 initial debris setup for our experiment, and more details are available in Fig. 5.

132
 133 The instrumentation consisted of nine surface piercing wire resistance wave gages (wg1 – wg9), eight
 134 ultrasonic wave gages (USWG1 – USWG8), and seven acoustic-Doppler velocimeters (ADV1 – ADV7).
 135 Seven of the USWGs and all of the ADVs were installed on the movable bridge, originally located over the
 136 slope (indicated by a dotted rectangle with sensor locations in Figure. 1a). USWG8 was installed at the end
 137 of the flat section. The movable bridge was fixed during the debris transport test and it was shifted 7.23 m
 138 forward (x-direction) to measure the kinematics conditions (surface elevation and velocity) at the flat
 139 section without debris cases (indicated by the second dotted rectangle in Figure 1a). The shifted location
 140 for seven USWGs and ADVs, which were installed on the movable bridge, are marked as USWG_h and
 141 ADV_h in Figure 1a. Table 2 summarizes the coordinates of the instrumentation. Note that the wavemaker
 142 displacement (wmdisp) was also recorded for all tests and is not used for this paper but is available for
 143 future numerical modeling efforts. Also, note that ultrasonic wave gages locations are reported for the two
 144 cases, for the debris transport tests and the kinematics tests in parenthesis.

145

146

Table 2. Instrument locations

Instrument description	Instrument	x (m)	y (m)	z (m)
Wavemaker displacement	wmdisp	-	0.00	-
Resistive wave gage	WG1	14.052	-3.540	-
Resistive wave gage	WG2	14.048	-0.056	-
Resistive wave gage	WG3	14.039	2.473	-
Resistive wave gage	WG4	14.341	2.482	-
Resistive wave gage	WG5	14.899	2.477	-
Resistive wave gage	WG6	15.394	2.474	-
Resistive wave gage	WG7	16.688	2.470	-
Resistive wave gage	WG8	19.278	-3.538	-
Resistive wave gage	WG9	19.246	2.494	-
Ultrasonic wave gage	USWG1 (USWG _h 1)	26.708 (33.941)	0.024 (0.024)	2.294 (2.294)
Ultrasonic wave gage	USWG2 (USWG _h 2)	26.701 (33.931)	0.498 (0.498)	2.302 (2.302)
Ultrasonic wave gage	USWG3 (USWG _h 3)	26.750 (33.973)	1.502 (1.502)	2.309 (2.309)
Ultrasonic wave gage	USWG4 (USWG _h 4)	26.757 (33.976)	1.992 (1.992)	2.305 (2.305)

Ultrasonic wave gage	USWG5 (USWG _h 5)	28.298 (35.531)	-0.003 (-0.003)	2.357 (2.357)
Ultrasonic wave gage	USWG6 (USWG _h 6)	28.286 (35.516)	0.523 (0.523)	2.428 (2.428)
Ultrasonic wave gage	USWG7 (USWG _h 7)	29.878 (37.111)	0.037 (0.037)	2.376 (2.376)
Ultrasonic wave gage	USWG8	40.655	-1.039 (-1.039)	1.769
Acoustic-Doppler Velocimeter	ADV1 (ADV _h 1)	26.715 (33.949)	-0.019 (-0.019)	1.020 (1.020)
Acoustic-Doppler Velocimeter	ADV2 (ADV _h 2)	26.705 (33.935)	0.479 (0.479)	1.049 (1.049)
Acoustic-Doppler Velocimeter	ADV3 (ADV _h 3)	26.736 (33.959)	1.494 (1.494)	1.053 (1.053)
Acoustic-Doppler Velocimeter	ADV4 (ADV _h 4)	26.735 (33.954)	1.992 (1.992)	1.041 (1.041)
Acoustic-Doppler Velocimeter	ADV5 (ADV _h 5)	28.296 (35.530)	-0.026 (-0.026)	1.018 (1.018)
Acoustic-Doppler Velocimeter	ADV6 (ADV _h 6)	28.290 (35.520)	0.473 (0.473)	1.011 (1.011)
Acoustic-Doppler Velocimeter	ADV7 (ADV _h 7)	29.867 (37.101)	-0.018 (-0.018)	1.018 (1.018)

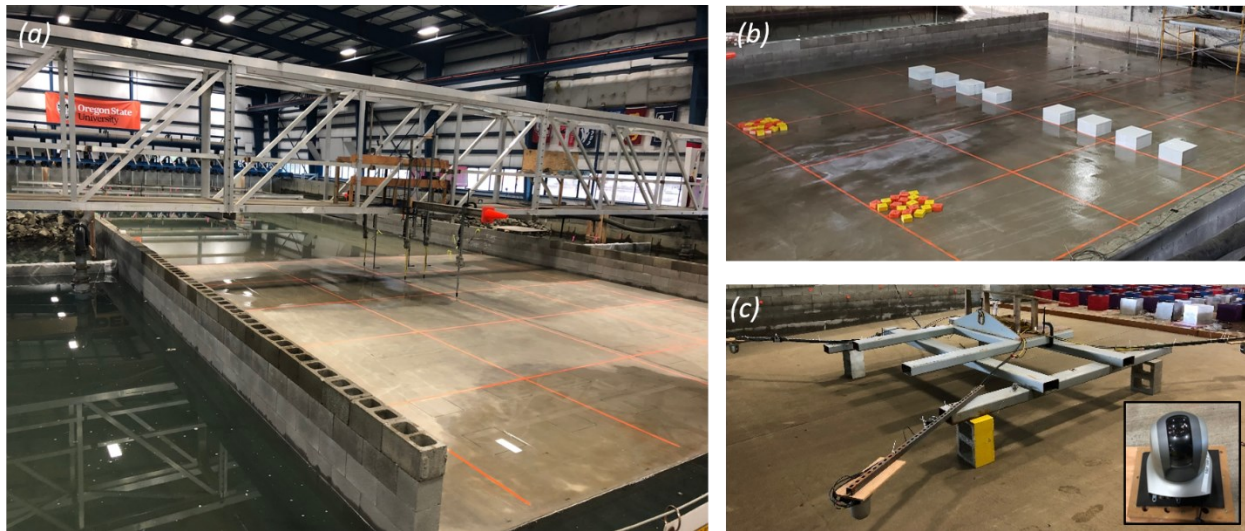
147

148 Figure 2 shows three photographs of the testbed and instrumentation. Figure 2a shows a general view of
 149 the testbed without debris and the movable bridge on the flat section and Figure 2b shows an example of a
 150 debris test setup using two groups of debris and eight obstacles (white boxes). Figures 2a and 2b show the
 151 two sidewalls in the flat section as well as the end of the test section that allowed the overland flow to spill
 152 into the basin. The orange grid lines in Figure 2a, 2b were painted with 2 m spacing to provide a frame of
 153 reference for the video cameras. Figure 2c shows the mounting device for four video cameras. These
 154 cameras were mounted on a steel frame and elevated at the center of the flat section to record the debris
 155 transport for all trials. The cameras are referred to as CAM1, CAM2, CAM3, and CAM4 (Fig. 1a) and had
 156 an overlapping field of view of a diagonal quarter of the flat region. The framerate of each camera was set
 157 at 29.97 Hz, and each camera had a resolution of 1080 by 1920 pixels. The facility lighting was controlled
 158 to provide optical contrast between the debris and to minimize the reflection from the water.

159

160 The debris was constructed from two types of material, high-density polyethylene (HDPE, painted orange)
 161 and Douglas-fir (wood, painted yellow) to study the different densities on debris transport (Fig. 3). The
 162 debris pieces measured 10.2 cm (*L*) by 10.2 cm (*W*) and 5.1 cm (*H*). About a 10 cm debris length scale was
 163 chosen based on an approximate geometric scale of 1:50 for this experiment. At this scale, the modeled
 164 debris would correspond to a prototype size of approximately 5 m which would be larger than a passenger
 165 vehicle and smaller than a shipping container. These are the two classes of debris considered, for example,
 166 in the engineering design of structures to withstand tsunami loads (e.g., Chock et al., 2016)

167

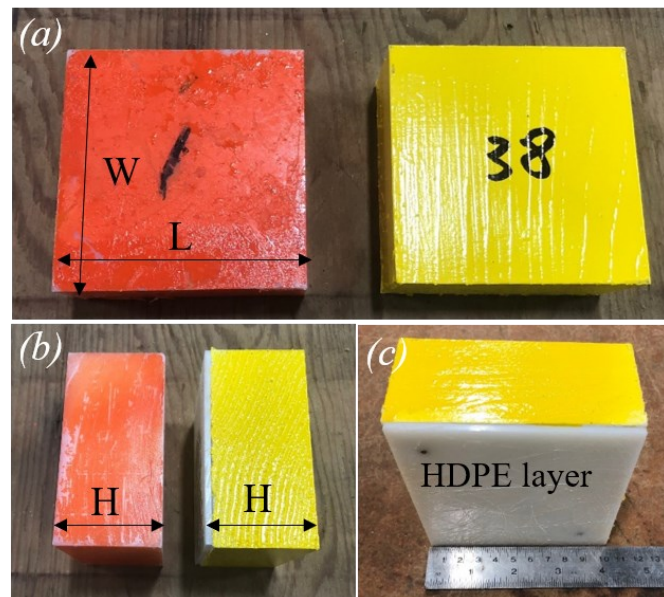


168

169 **Figure 2:** Photographs of the debris test setup. (a) Overview of the testbed without debris,
 170 (b) Overview of the testbed in other direction with two sets of debris and eight obstacles,
 171 (c) Steel frame for the camera mounting and snapshot of the camera (inner photo).

172

173 Although geometric similitude has been used to describe the size of the debris, we did not attempt to scale
 174 the density or proper center of gravity of the debris for debris such as shipping containers or vehicles. As
 175 noted by one of the reviewers, the detailed motion of the debris under real-world conditions for these debris
 176 types would require careful consideration of the correct specific gravity and center of gravity.



177

178 **Figure 3:** (a) Plan view of HDPE (orange) and Wood debris (yellow), (b) Side views (c) HDPE layer
 179 (2.5mm) for Wood debris. Both HDPE and wood debris have the same size.

180

181 During preliminary tests, we observed that the motion of the debris was sensitive to the friction between
 182 the bottom of the debris and the concrete floor of the test section. Further, we observed that the wood debris

183 would become worn during these tests, unlike the HDPE which became scratched initially and then
184 remained fairly consistent without additional wear. To keep the surface roughness the same between the
185 two debris types and to prevent changes in the surface of the wood debris during multiple trials, we removed
186 a 2 mm layer from the bottom of the wood debris and replaced it with the same thickness of HDPE. Both
187 the HDPE and wood debris were roughened on the concrete surface to create a consistent physical
188 roughness for all debris elements before starting the final experiments presented here.

189

190 The measured mean density of HDPE and wood debris was 987 (11.7) kg/m^3 and 648 (17.6) kg/m^3 ,
191 respectively, after painting. The standard deviation is presented in parenthesis. The weight of each HDPE
192 and wood debris was 0.524 kg and 0.326 kg , and the draft of each HDPE and Wood debris was 5.03 cm
193 and 3.30 cm , respectfully. The wood debris was wiped dry at the end of each day and reweighed to
194 determine whether the density changed during the testing. We observed less than 2 % change in density of
195 the wood debris throughout the testing which lasted several days. We maintained the same initial conditions
196 on the test section by manually removing water on the test surface using floor squeegees after each trial,
197 and then it took an additional 10 minutes to set up the next tests. Therefore, the concrete itself was wet
198 before each trial as can be seen in Figure 2b, but there were no areas with measurable standing water before
199 testing.

200 The static friction coefficient (μ_s) was measured for both debris types under the slightly wet conditions of
201 the test section using $F = \mu_s N$ where F is the horizontal force and N is the normal force. We connected a
202 small load cell to individual pieces of debris and then applied a horizontal force until the debris started to
203 move. These tests were conducted at 16 locations within the 10 m by 10 m test section and were repeated
204 3 times at each location for a total of 48 tests for each debris type. The averaged static friction coefficient
205 and standard deviations under the test conditions were $\mu_s = 0.66$ (0.07) for HDPE and $\mu_s = 1.28$ (0.13) for
206 wood, with the standard deviation in parenthesis. The measured friction coefficient is an important
207 parameter of future numerical modeling of debris transportation, as the friction coefficient will be decisive
208 in comparing experimental and numerical results. It is noted that the coefficient of friction for the wood
209 debris is nearly double that of the HDPE debris, even though the wood debris has the same HDPE material
210 on the bottom. This difference is likely due to surface tension effects between the debris and the concrete
211 which was not considered when estimating the friction coefficient.

212

213 **3. Experimental Procedure**

214

215 **3.1 Water depth and Wave conditions**

216 To reduce the overall complexity of the experiments, we performed all tests using the same water level
217 and wave condition (wavemaker displacement time series). To arrive at an appropriate depth and wave
218 condition, we tested several waves and water depth conditions to meet four criteria. First, we wanted a
219 relatively long inundation period and flow conditions with a Froude number of $Fr \sim 1.0$ based on numerical
220 simulations of tsunami inundation flow (e.g., Park et al., 2018). Second, we wanted to avoid a breaking
221 wave directly on or in front of the debris because the splash up and generation of air bubbles could
222 interfere with the optical measurement. Moreover, this type of entrainment mechanism may be less
223 common based on the video of debris transported during the 2011 Tohoku tsunami. Third, we wanted the
224 debris to come to rest within the 10 m test section without having the debris wash over the end ($x = 42 m$).
225 Fourth, for simplicity, we wanted to avoid reflected waves that could have been large enough to cause
226 subsequent motion to the debris.

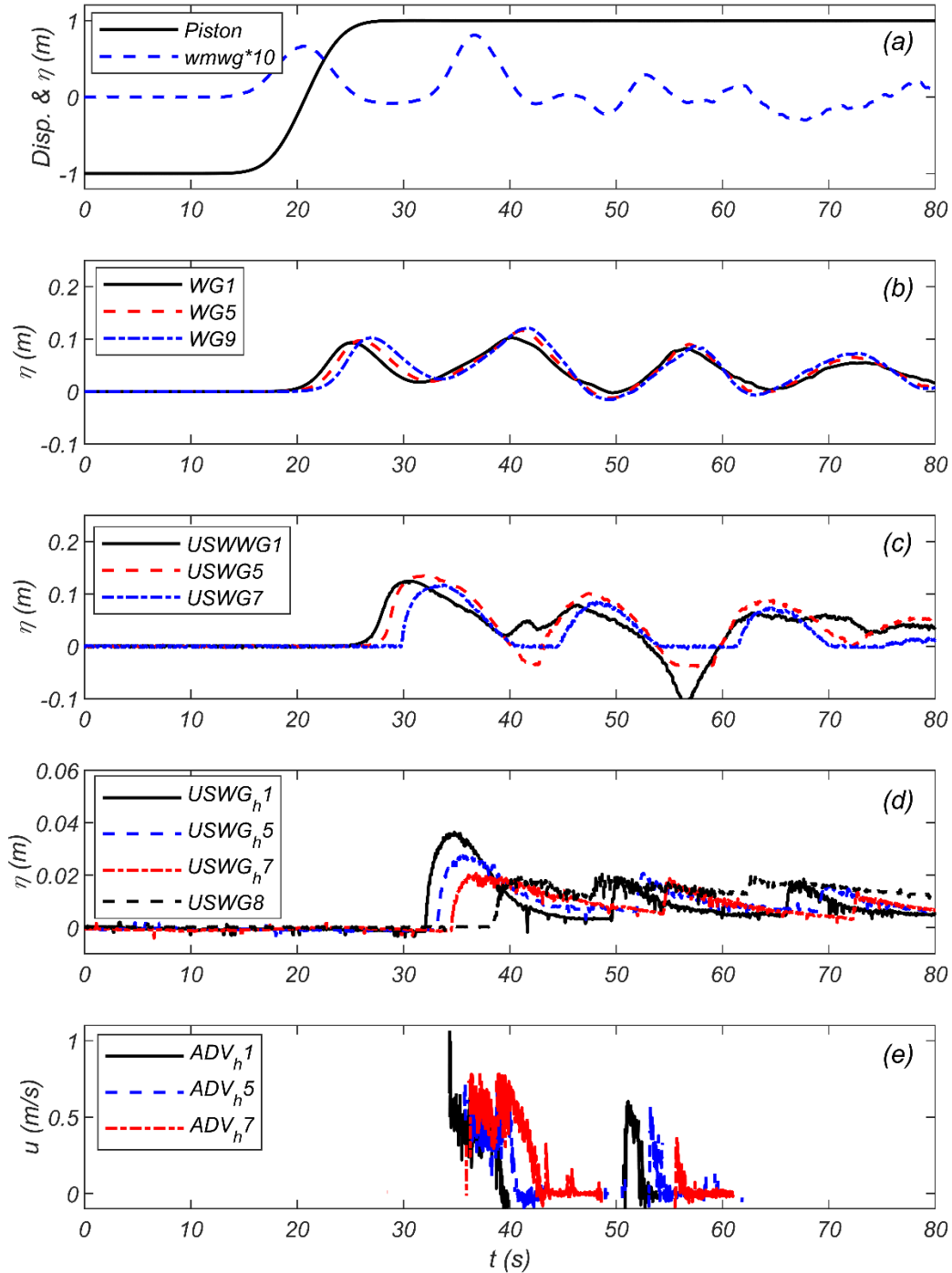
227 After trial and error, we arrived at a condition with a fixed water depth ($z = 0.78 m$) and the wavemaker
228 displacement time series as shown in Figure 4a (solid black line) based on previous experiments in this
229 facility for tsunami inundation (e.g., Park et al., 2013) and debris impact (e.g., Ko et al., 2015). Figure 4a
230 also shows the fluctuation of surface elevation (η) at the wavemaker (*wmwg*, dashed blue). The wavemaker
231 displacement time series was determined using an error function rather than solitary wave theory so that
232 we could maximize the full, 2 m stroke of the wavemaker. Then, the time of the wavemaker displacement
233 was adjusted to achieve the conditions described earlier. The second peak at $t \sim 37 s$ is the wave reflected
234 from the test section reaching the wavemaker. Active absorption was not used, so the reflected wave was
235 re-reflected from the wavemaker and inundated the test section a second time. However, the amplitude of
236 this second inundation was much smaller than the first and did not cause any further displacement of
237 debris.

238 Figure 4b, c, and d show how the free surface profile varies as the initial wave propagates over the slope
239 (4b and 4c) and at the flat region (4d). The maximum measured amplitude occurred at USWG 5 ($h_{max} =$
240 $0.14 m$) before the water shoreline at $x = 31.29 m$. The period of the positive amplitude surface elevation
241 was 11.1 s at *wg1* and increase to 13.2 s at USWG 5. As the wave inundated over the testbed, the maximum
242 amplitude decreased, and inundation duration increased as can be seen in Figure 4d. Considering the draft
243 of each HDPE (5.03 cm) and wood (3.30 cm) debris, the entrained HDPE debris will start grounding before
244 reach to the USWG_h 1 ($x=33.941 m$), while wood debris will start grounding around at USWG_h 5 ($x =$
245 $35.531 m$).

246 The corresponding velocity of the wave in the x -direction from ADV shows that the measured peak velocity
247 was about 1.0 m/s at USWG_h1 and ranged from 0.55 to 0.65 m/s at USWG_h5, and USWG_h7. (Fig. 4e). The
248 estimated Froude number at the peak amplitude from USWG_h1 to USWG_h7 ranged from $Fr = 1.11$ to Fr
249 = 0.71. It is noted that ADV sensors could not capture leading-edge flow successfully (e.g., Park et al.,
250 2013), and data are discontinued because of relatively low surface elevation. Later, we use the optical
251 measurements to infer the velocity of the leading edge.

252 We acknowledge that the overall inundation duration time is too short compared to a tsunami at the
253 prototype scale. So, these tests represent only an idealized model of tsunami inundation. Future
254 experiments should consider tsunami inundation with longer durations.

255



256

257 **Figure 4:** Time series of (a) displacement of piston and surface elevation at the wavemaker, surface
 258 elevation over the slopes by (b) wire resistance wave gages (WG) and (c) ultrasonic wave gages (USWG),
 259 (d) surface elevation at the flat test region by ultrasonic wave gages (USWG_h), and (e) measured x-
 260 directional velocity at ADV_h.

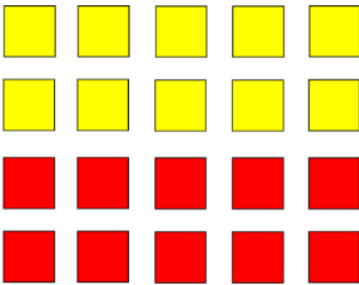
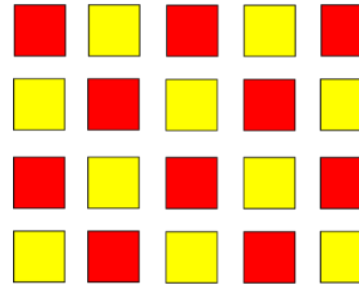
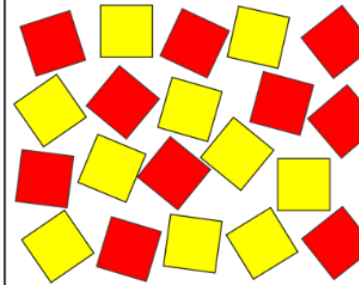
261

262 **3.2. The initial position of grouped debris and test case**

263 The processes of the initial debris entrainment and subsequent transport could be affected by the number
 264 and arrangement of debris elements (e.g., Goseberg et al., 2016; Nistor et al., 2017b; Stolle et al., 2017).
 265 For example, the spacing between debris elements or the location of the debris field itself relative to the
 266 shoreline could also affect the debris transport phenomena. To decrease the number of permutations and to
 267 focus our study on debris density and obstacles, we chose to keep the number of debris elements constant
 268 ($N = 20$), while previous studies had utilized series of different number of debris up to eighteen as a grouped
 269 debris (Nistor et al., 2017). Twenty elements were seen as a reasonable number to have confidence in the
 270 measured mean locations and to reproduce debris-debris contact that could influence their trajectories and
 271 final locations. Further, we kept the initial location of the debris field fixed to allow comparison among
 272 trials and to avoid having to change the camera setup. The debris field location was chosen at the leading
 273 edge of the flat test section ($x = 31.29\text{ m}$).

274 We kept the overall footprint of the initial debris field constant. For this, we utilized a 71.4 cm by 56.1 cm
 275 frame so that we could place a matrix of 5×4 debris elements with a gap spacing of $\alpha = 5.1\text{ cm}$ between
 276 each element within this frame. The frame was removed prior to the start of the tests. With this frame, we
 277 used three configurations for the initial debris position: Uniform (C1), Checker (C2), and Random (C3) as
 278 shown in Figure 5. The Uniform and Checker configurations had 4 rows and 5 columns and constant gap
 279 spacing (α). The Random configuration consisted of the 20 debris elements within the frame at irregular
 280 orientations and spacings between the debris. The Checker configuration was used only with an equal mix
 281 of 10 HDPE and 10 wood debris elements. The Uniform and Random configurations were used with
 282 different levels of mixed debris.

283 The 10 m wide test section allowed for two debris groups to be tested simultaneously without interference
 284 by the adjacent tests. This was based on a number of preliminary tests and confirmed by checking for bias
 285 in the results presented here. The two test sections are termed as Region A and Region B, whose centroids
 286 are located at $y = -2.0\text{ m}$ and $y = 2.0\text{ m}$ as shown in Figure 2b.

C1	C2	C3
Uniform	Checker	Random
		

288 **Figure 5:** Example sketch of three configurations of a debris group, C1 (uniform), C2 (checker), and C3
 289 (random).

290

291 Table 3 summarizes the debris experiment cases, trials, and configurations. Column 2 denotes the debris
 292 configuration used, and Column 3 indicates the number of obstacles N_{obs} added in the test section. Cases
 293 1-10 had no obstacles, and Cases 11 – 18 systematically increased N_{obs} in even increments from 2 to 6 for
 294 each region. Column 4 indicates the number of repeated trials for each case, N_r , and it is noted that not all
 295 trials could be repeated because of time constraints. In total, there were 45 trials conducted in two regions
 296 for a total of 90 tests. Column 5 shows the ratio of the gap distance to the characteristic debris length, a/L .
 297 Cases 1-4 were essentially pilot tests to determine whether this ratio had any effect on the overall tests, and
 298 it was observed that there was essentially no significant effect on the dislocation of debris for $0.25 < a/L <$
 299 2.0. Therefore, $a/L = 0.5$ was used consistently for Uniform and Checker cases. The remaining columns
 300 show the number of HDPE and wood debris elements and the resulting specific gravity of the debris group
 301 SG_g in each region for each case. We considered debris groupings of 100% of one type, and mixes of
 302 25%/75%, 50%/50%, and 75%/25% so that SG_g varied 0.65 (wood only), 0.74, 0.84, 0.91, and 0.99 (HDPE
 303 only). For example, Figure 2b shows a trial for Case 16 with a Random (C3) configuration, 4 obstacles,
 304 and an equal mix of debris elements in Region A and B ($SG_g = 0.84$). The specific gravity (SG) represents
 305 the density (materials) condition of debris, and it is relatively convenient to be determined rather than the
 306 draft of debris, which is required to exact the shape (Volume) of debris. The grouped specific gravity (SG_g)
 307 could represent the effects of different density (materials) conditions on debris transportation as a group.
 308 Additionally, this dimensionless value is extendible to other applications such as the probabilistic approach
 309 on the multi-debris motions (interactions) or debris collision ratio to obstacles while debris transport as a
 310 group.

311 The fixed obstacles seen as gray boxes in Figure 2b were 0.4 m by 0.4 m with 0.3 m height concrete blocks.
 312 The size of these obstacles was chosen to represent structures in the built environment such as commercial
 313 buildings that could affect the tsunami flow field. At a 1:50 geometric case, these obstacles would be 20 m
 314 wide in prototype, and the 400 m² prototype area is approximately the footprint of a popular US fast-food
 315 franchise or a small hotel. The row of obstacles was located 4 m from the initial debris field (200 m
 316 prototype) and could be considered a parking lot with passenger vehicles or container storage yard with
 317 shipping containers. The spacing between obstacles was 0.4 m (20 m prototype), the same as the length
 318 scale of the obstacles themselves. This facilitated the symmetrical placement of obstacles such that the case
 319 of $N_{obs} = 8$ obstacles had 12 total obstacles uniformly across Region A and B (note that 12 obstacles and 13
 320 gaps at 0.4 m each equals the 10 m spacing of the test section). The middle four obstacles were common
 321 to both Region A and B.

322 **Table 3:** Description of debris experimental trials.

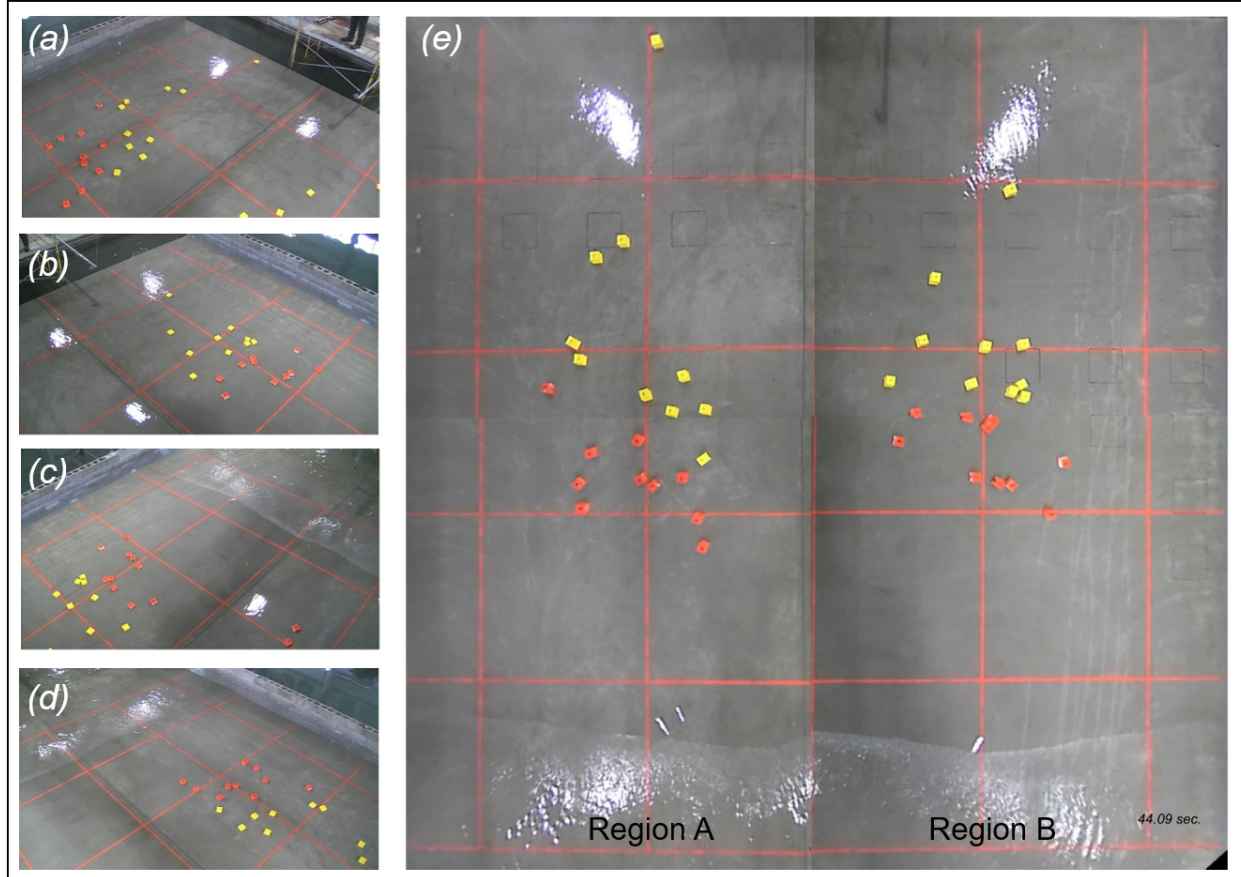
Case	Debris Config.	N_{obs}	N_r	α/L	Region A			Region B		
					HDPE (number)	Wood (number)	SG_g	HDPE (number)	Wood (number)	SG_g
1	C1	0	1	0.5	20	0	0.99	—	—	—
2	C1	0	1	0.5	20	0	0.99	0	20	0.65
3	C1	0	1	2.0	20	0	0.99	—	—	—
4	C1	0	1	0.25	20	0	0.99	—	—	—
5	C1	0	2	0.5	15	5	0.91	5	15	0.74
6	C1	0	1	0.5	10	10	0.82	10	10	0.82
7	C2	0	1	0.5	10	10	0.82	10	10	0.82
8	C3	0	7	0.5	10	10	0.82	10	10	0.82
9	C1	0	2	0.5	5	15	0.74	15	5	0.91
10	C1	0	1	0.5	0	20	0.65	20	0	0.99
11	C3	2	4	0.5	20	0	0.99	0	20	0.65
12	C2	2	5	0.5	10	10	0.82	10	10	0.82
13	C3	2	7	0.5	10	10	0.82	10	10	0.82
14	C3	2	1	0.5	0	20	0.65	20	0	0.99
15	C2	4	1	0.5	10	10	0.82	10	10	0.82
16	C3	4	3	0.5	10	10	0.82	10	10	0.82
17	C2	8	3	0.5	10	10	0.82	10	10	0.82
18	C3	8	3	0.5	10	10	0.82	10	10	0.82

323

324 **3.3. Correction and rectification of video images**

325 Figure 6a to d shows an example field of view from each of the four cameras for the same trial. To correct
 326 for lens distortion, we collected a number of black and white checkerboard images with a 0.1 m unit width
 327 throughout the test section. We utilized these images to extract the camera correction parameters using the
 328 ‘undistortImage.m’ provided in the camera calibration app from the Matlab toolbox and applied them to
 329 our raw recorded images. The estimated overall mean error was less than 3 pixels for all four cameras,
 330 which is equivalent to about 3 cm . After the lens correction, the images were rectified through
 331 ‘fitgeotrans.m’, which utilizes the surveyed locations of the orange gridline intersections on the test section.

332 Finally, the four rectified images were merged and trimmed into a single image to cover the test region.
 333 Figure 6e shows the example result for Case 6 with a uniform mix of debris (10 HDPE and 10 Wood)
 334 without obstacles. This was repeated for the final debris position for all trials for subsequent analysis in
 335 Section 4.1 and 4.2. For nearly all trials, this process was repeated frame-by-frame to provide continuous
 336 video for the debris velocity analysis in Section 4.3.



337
 338 **Figure 6:** Example snapshots of recorded video images of Case 6. (a) to (d) A raw video image from CAM1
 339 to CAM4. (e) A rectified and merged image for Case 6.
 340

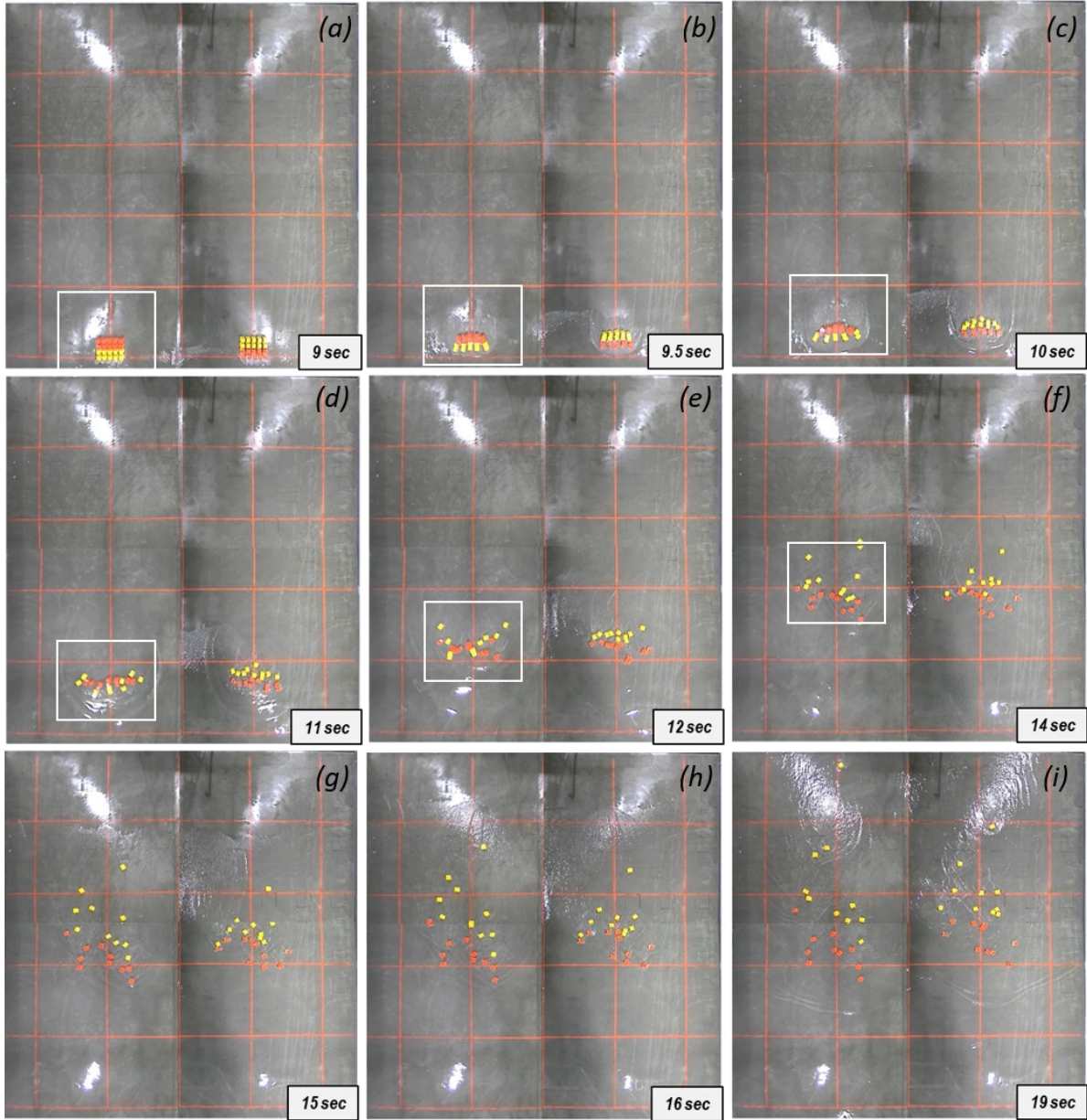
341 **3.4. Optical measurement of debris transport.**

342 Figure 7 shows a series of video images from Case 6. Debris groups in Region A and B use a uniform (C1)
 343 configuration with an equal mix of HDPE and wood elements. The initial debris configurations are slightly
 344 different with HDPE placed in the first and second rows in Region A and the third and fourth rows in
 345 Region B. At the time of $t^* = 9$ s, the leading edge of the tsunami-like wave reaches the initial debris field,
 346 and by $t^* = 19.0$ s, all debris has reached their final location. Here, t^* is the time frame corresponding to
 347 the video recording, where $t^* = 0$ is the manual start of the video recorder and corresponding to the
 348 wavemaker motion at $t = 16$ s in Figure 4a. In general, the debris was entrained by the leading edge of the

349 flow and started moving, initially dragging on the bottom until the flow depth was sufficient for the buoyant
350 force to fully float the debris. Then the debris was transported smoothly over the testbed, although some
351 debris-debris collision, subsequent dragging, and interactions were observed as will be described later. The
352 white boxes indicate detailed regions shown in Figure 8.

353 The effect of density can be seen in these images, where the less dense debris (wood, yellow) is transported
354 much further in the flow direction (x-direction) over the test section. The major difference in the debris
355 transport between two different debris elements is caused by the different draft conditions of HDPE (5.03
356 cm) and wood debris (3.30 cm) and relative flow depth changes over the testbed. As mentioned earlier, the
357 HDPE debris is grounded earlier than the wood debris, and, consequently, the grounded HDPE disturbs the
358 downstream flow fields and debris motions.

359 Although there is some variation among the final location for the ten elements of either density, there is
360 almost no overlap among the debris types in the x-direction. Interestingly, although the initial placement
361 of the debris elements was reversed in Region A and B, the sequence of images shows how the lighter
362 density (yellow) objects move past the higher density objects in Region A around $t^* = 12$ s. By $t^* = 14$ s,
363 all of the lighter density objects are further in the x-direction compared to the denser objects in Region A.
364 These lighter objects are in a similar position to their counterparts in Region B, indicating the effects of the
365 initial debris configuration are short-lived for these experiments.



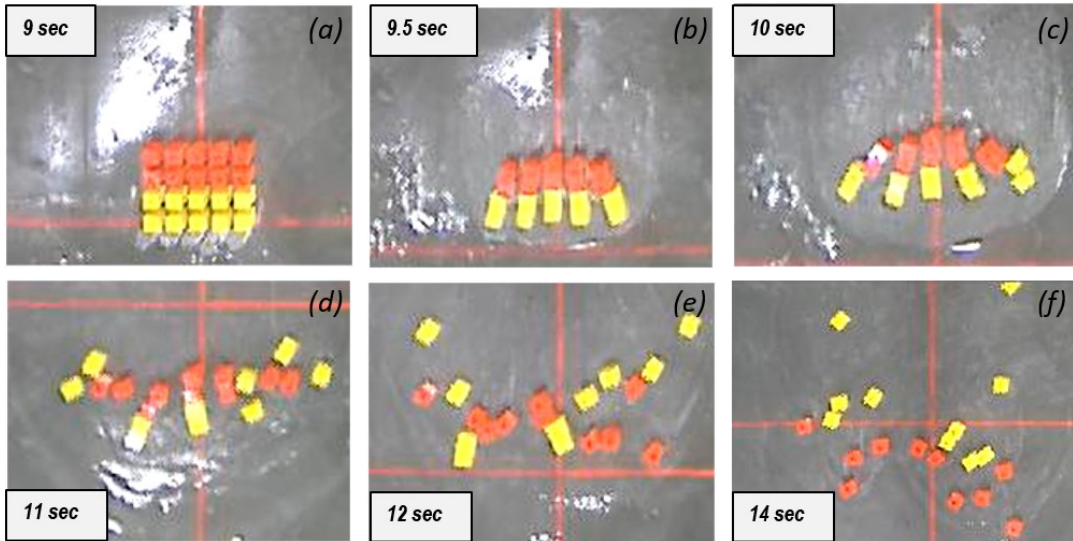
366

367 **Figure 7:** Series of images showing debris entrainment and transport for Case 6.

368

369 Figure 8 shows the details of the initial entrainment and transport process for Region A highlighted in the
 370 previous figure. Initially, as the tsunami reaches the debris field, the gaps between the debris are closed ($t^* = 9.5$ s). Five columns are formed and bend radially, matching more or less the radial wavefront seen in the
 371 images. This motion was also observed at a larger scale by Rueben et al. (2015) and by Nistor et al. (2017b).
 372 Ultimately, the columns become unstable ($t^* = 11$ s), beginning with the outer columns moving toward the
 373 middle column. This destabilization of the column is also observed in the uniform debris case, although the
 374 column becomes destabilized more quickly in the case of debris with uniform density. In any case, the
 375 column becomes destabilized more quickly in the case of debris with uniform density. In any case, the

376 lighter debris field moves through the heavier field ($t^* = 12$ s and 14 s). The light debris on the left-most
 377 column flows rather easily to the left of the two heavier debris pieces ahead (Fig. 8d), and a mirror image
 378 of that occurs on the rightmost column. The light debris in the three middle columns experiences some
 379 debris-debris collision (Fig. 8e). Rather quickly, the debris fields become separated with the outer debris
 380 pieces moving much further along in the flow (Fig. 8f).



381 **Figure 8:** Detail from Figure 7 of the entrainment and transport process in Region A.

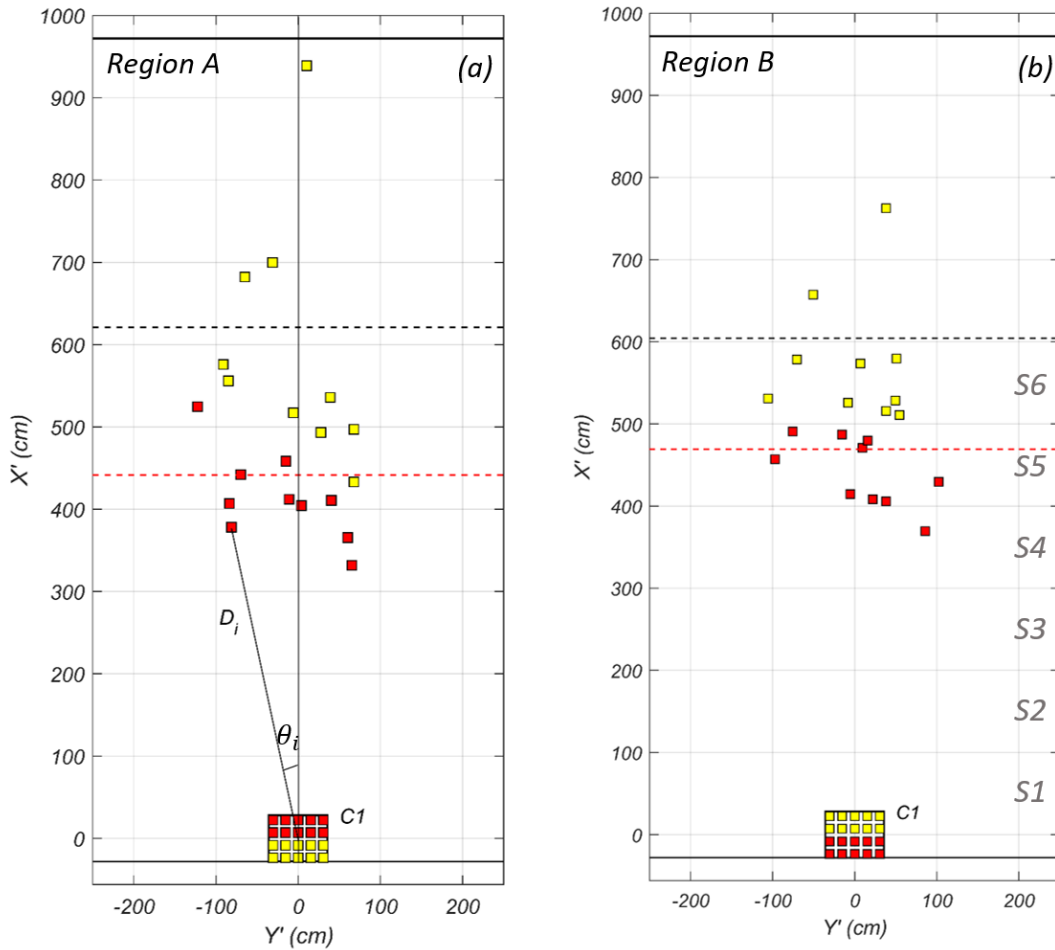
382
 383
 384 It is worth noting that not all debris elements moved with constant velocity for all tests, with some debris
 385 elements experiencing local acceleration or deceleration due to the local changes of flow field between
 386 adjacent debris, debris-debris collision, and interaction with the concrete floor with changes in flow depth.
 387 This was also observed by Rueben et al. 2015 (see, for example, their Figure 13c) during some, but not all,
 388 of their repeated trials, suggesting that this temporary grounding may be due to slight variabilities in the
 389 flow field, particularly the wakes that are generated during debris entrainment. In general, though, the
 390 lighter (wood) moved more uniformly and much further in the x -direction when it was not impeded by
 391 heavier (HDPE) debris.

392 **3.5. Quantification of final debris location.**

393 Figures 9a and b show the initial and final debris locations in Region A and Region B for the same case
 394 shown in Figure 7 where the X' and Y' are the new Cartesian coordinates with the origin at the center of the
 395 debris frame ($x = 31.65$ m, $y = -2.0$ m in Region A and $x = 31.65$ m, $y = 2.0$ m in Region B). The final
 396 displacement of the i -th debris (D_i) and its spreading angle (θ_i) from the center of the debris frame was
 397 calculated. The red and black dashed lines indicate the mean longitudinal distance of HDPE and wood
 398 debris, respectively, which are calculated as

399 $\overline{D'_X} = (\sum_i^n D_i \cos \theta_i)/n$ (1)

400 where n is the total number of HDPE or wood debris elements used in each case. Comparing Region A and
 401 B, the mean longitudinal distance of HDPE and wood debris is not sensitive to the initial positioning of
 402 debris, even though the details of the entrainment and transport processes shown in Figure 7 were different.
 403 In addition to the displacement, we used the video images to estimate the debris velocity in the X' direction
 404 across 100 cm intervals and marked them as $S1, S2, S3, S4, S5$, and $S6$ in Figure 9b.



405

406 **Figure 9:** Digitized results of the case with $SG_g = 0.82$ (Case 6, Fig. 7) at initial debris position ($t^* = 0$ s)
 407 and the final stage ($t^* = 19$ s). (a) at Region A, and (b) at Region B. The red and yellow square indicates
 408 the location of HDPE and wood debris, respectively, and red and black dashed lines indicate the mean
 409 longitudinal distance of HDPE and wood debris, respectively.

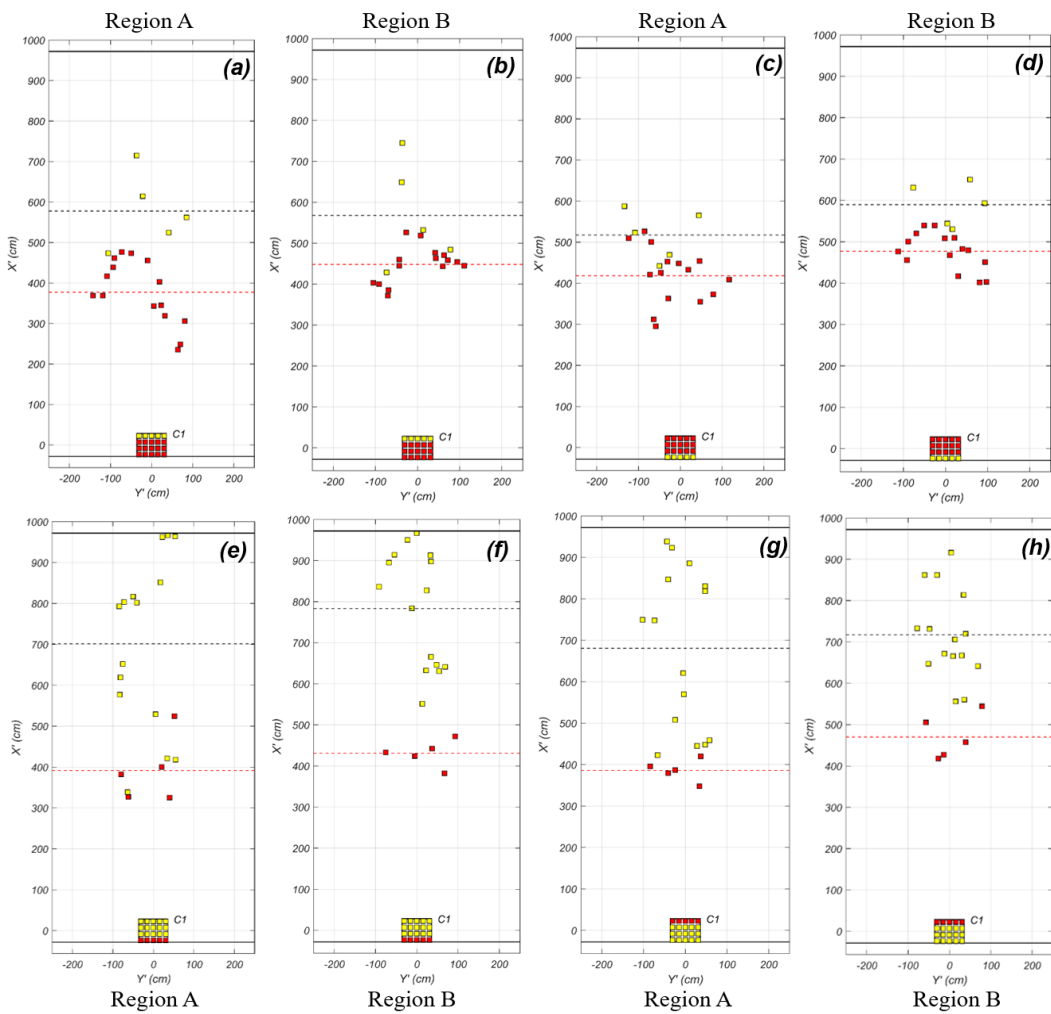
410

411 **4. Results of debris advection**

412

413 **4.1 Longitudinal distance of debris**

414 Figure 10 shows the results of two different SG_g conditions with two different initial positions of HDPE
 415 and wood in Region A and B. The upper panels (Fig. 10a, b, c, d) present the case of SG_g is 0.91 (Case 5)
 416 composed of 15 HDPE and 5 wood elements, and the lower panels (Fig. 10e, f, g, h) present the case of
 417 SG_g is 0.73 (Case 9) with 5 HDPE and 15 wood elements. The tests utilized the Uniform (C1) configuration,
 418 and the left four panels (Fig. 10a, b, e, f) present cases where the wood debris is landward of the HDPE,
 419 while the right four panels (Fig. 9c, d, g, h) present the opposite case of the wood on the seaward side of
 420 the HDPE. Lastly, the same initial debris positions are repeated at each Region A (Fig. 10a, c, e, g) and
 421 Region B (Fig. 10b, d, f, h).



422

423 **Figure 10:** Initial and final debris locations for Case 5 (upper panels) and Case 9 (lower panel). (a) to (d)
 424 present 15 HDPE and 5 wood elements (Case 5) with different initial debris configuration and at two
 425 different regions (Region A and B). (e) to (h) present 5 HDPE and 15 wood elements (Case 9).

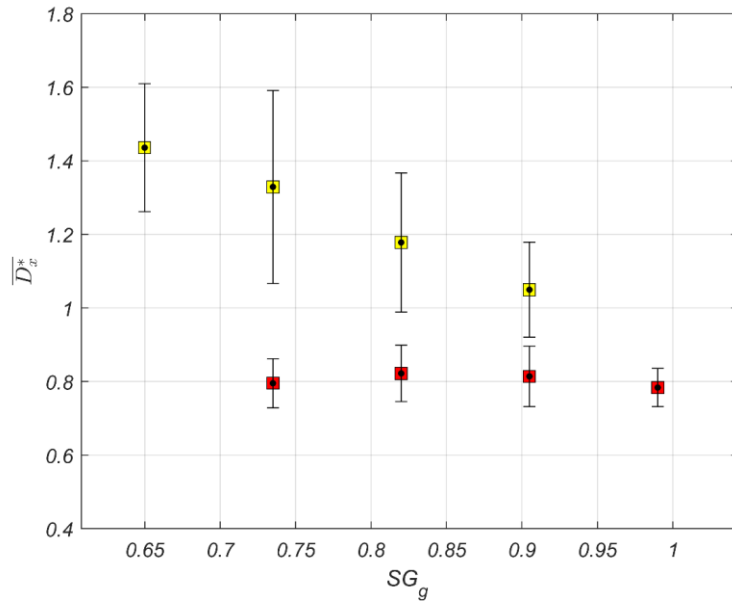
426

427 For the top panels (Fig. 10 a, b, c, d), the mean longitudinal distance (\bar{D}'_x) of the wood debris ranges from
 428 510 to 590 cm and is approximately 31% further than the HDPE debris elements in the range 390 to 480
 429 cm. For the bottom panels (Fig. 10 e, f, g, h), \bar{D}'_x of the wood, debris elements range from 690 to 790 cm
 430 and are approximately 72% further than the HDPE in the range 390 to 470 cm. Two major observations
 431 can be made. First, as was noted in Figure 7, \bar{D}'_x is independent of the initial orientation of the debris:
 432 whether the wood debris was landward or seaward of the HDPE did not affect \bar{D}'_x for a given SG_g condition.
 433 Second, while there was a significant change in \bar{D}'_x for the wood debris due to different SG_g conditions,
 434 there was no significant change in \bar{D}'_x for the HDPE debris. In other words, \bar{D}'_x was much larger for the
 435 wood debris when the group consisted of 75% wood debris compared to 25% wood debris, but \bar{D}'_x was
 436 about the same for 75% HDPE as it was for 25% HDPE.

437 To generalize the effects of group density on the longitudinal distance, Figure 11 shows the mean
 438 longitudinal distance and the 95% of confidence interval for HDPE and wood debris for the five SG_g
 439 conditions from $SG_g = 0.65$ (wood only) to $SG_g = 0.99$ (HDPE only). For comparison, we plot \bar{D}^*_x defined
 440 as the mean longitudinal distance normalized by the mean longitudinal distance of Case 8 with $SG_g = 0.82$
 441 (equal number of HDPE and wood elements) and Random (C3) debris configuration. Case 8 was repeated
 442 seven times (Table 3), and the values used for normalization were $\bar{D}'_x = 4.51$ m for HDPE and $\bar{D}'_x = 6.99$ m
 443 for wood. It is noting that seven repeated trials only intended to check the repeatability of our experimental
 444 procedure. Figure 11 clearly shows that \bar{D}^*_x for the higher density debris (HDPE, red) is nearly constant
 445 ($\bar{D}^*_x \sim 0.8$) while \bar{D}^*_x for the lower density debris (wood, yellow) decreases linearly as SG_g increases. This
 446 linear decrease would extrapolate to approximately the same value of \bar{D}^*_x for the HDPE only case.

447 It is interesting to note that the variation in \bar{D}^*_x indicated by the 95% confidence limits (c.l.) are fairly
 448 uniform across all values of SG_g for HDPE, indicating that the presence of the lighter debris has little to no
 449 influence on the heavier debris. Moreover, the 95% c.l. is several times smaller than for the wood debris.
 450 On the other hand, the 95% c.l. for the wood debris increases as SG_g decreases, indicating that the presence
 451 of the heavier debris affects the variability in the final position of the lighter debris. Even a relatively small
 452 amount of heavier debris (25%) causes the variation in \bar{D}^*_x for the lighter debris for $SG_g = 0.73$ cases to be
 453 larger than the cases where only the lighter debris was present ($SG_g = 0.65$).

454



455

456 **Figure 11:** Normalized mean longitudinal distance, \overline{D}_x^* of HDPE and wood and debris as a function of
 457 SG_g . Vertical bars indicated a 95% confidence interval.

458

459 4.2 Spreading Angle of Debris

460 The spreading angle of debris is a key variable to estimate the region for potential tsunami debris impacts
 461 or debris damming from the initial debris site (e.g., ASCE 2016). Based on a field survey from the 2011
 462 Tohoku tsunami of debris from a shipping container yard, Naito et al. (2014) estimated the debris spreading
 463 angle as

$$464 \quad \theta = \pm 22.5^\circ \quad (2)$$

465 where $\theta = 0^\circ$ is defined perpendicular to the shoreline, and it was assumed that the tsunami inundation was
 466 also normally incident to the shoreline. Nistor et al. (2017b) conducted a small-scale physical model study,
 467 suggesting that the debris spreading angle increases as the number of debris elements increases. They found
 468 that

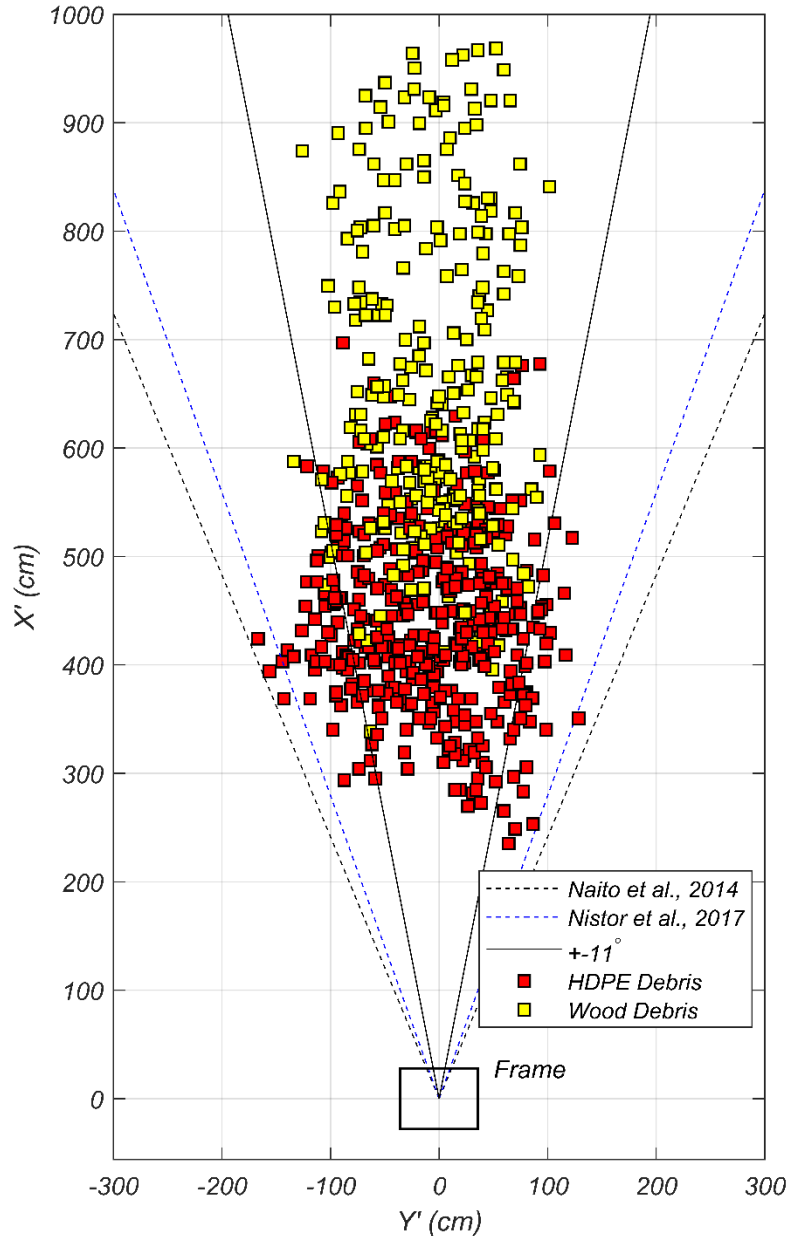
$$469 \quad \theta = \pm 3.69^\circ \pm 0.80 N \quad (3)$$

470 where N is the number of debris elements.

471 Figure 12 shows the spreading angle for all trials for Cases 1, Case 4 – Case 10 computed using Eq. 2, and
 472 Eq. 3 ($N = 20$, $\theta = \pm 19.69^\circ$). The denser debris (HDPE, red) shows a wider spreading angle and is bounded
 473 reasonably well by both equations. However, the less-dense debris (wood, yellow), which has a shallower
 474 draft (3.30 cm), has a narrower spreading angle, $\theta = \pm 11^\circ$, compared to the denser debris, which has a
 475 deeper draft (5.03 cm), highlighting the role that debris density could have in debris dispersion. Moreover,

476 Figure 12 shows that both equations are conservative in their estimates of debris spreading angle for the
 477 less dense debris.

478



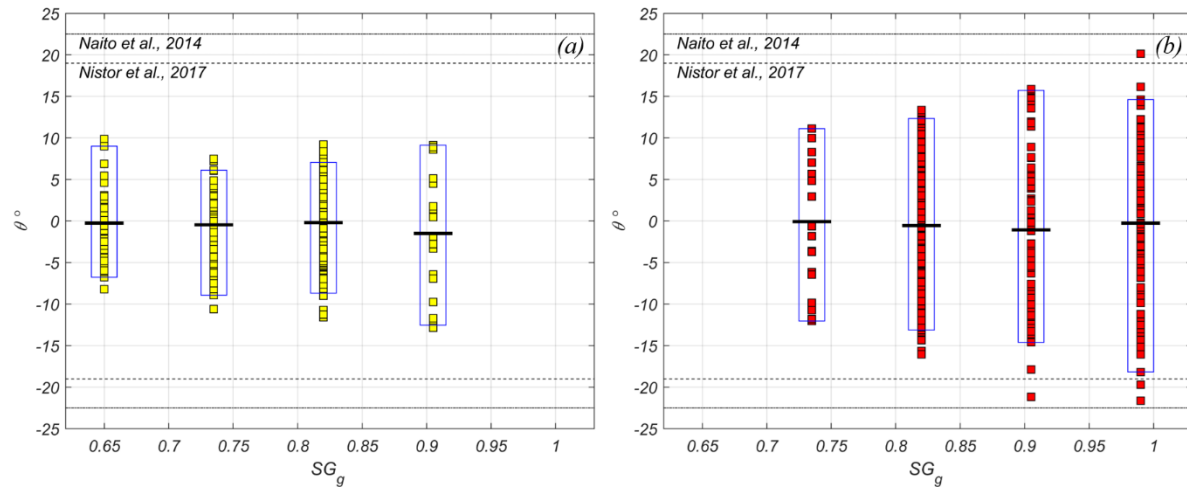
479
 480 **Figure 12:** Coordinate of debris from all trials for Case 1, 4 to 10. The solid box indicates that the frame
 481 we used for the initial position setup of debris. Each black and blue dashed line indicates the Spreading
 482 angle predicted by Eq. 2 (dashed black, Naito et al., 2014), Eq. 3 (dashed blue, Nistor et al., 2017b), and
 483 $\pm 11^\circ$ (solid black).

484

485 Figure 13 shows the spreading angle of wood (Figure 13a) and HDPE (Figure 13b) debris at the five SG_g
 486 conditions. In the figure, each colored box indicates the spreading angle (θ_i) of a single debris element in a

487 given trial at that SG_g condition, the black line shows the mean spreading angle across all trials, and a blue
 488 box indicates the 95% confidence interval, q_{95} . Overall, the spreading angle of wood debris is narrower
 489 than the predictions of Naito et al. (2014) and Nistor et al. (2017b) and is typically less than 10° . Overall,
 490 the spreading angle increases slightly for the less dense debris as SG_g condition increases.

491 Figure 13b for the HDPE debris shows a somewhat clearer trend of the spreading angle increasing as the
 492 SG_g condition increases. In any case, there is a clear distinction in the spreading angle for the wood only
 493 case ($SG_g = 0.65$, $-8^\circ < q_{95} < 10^\circ$) and the more dense HDPE cases ($SG_g = 0.99$, $-22^\circ < q_{95} < 20^\circ$).



494

495 **Figure 13:** Spreading angles of (a) wood debris and (b) HDPE debris at different SG_g conditions.

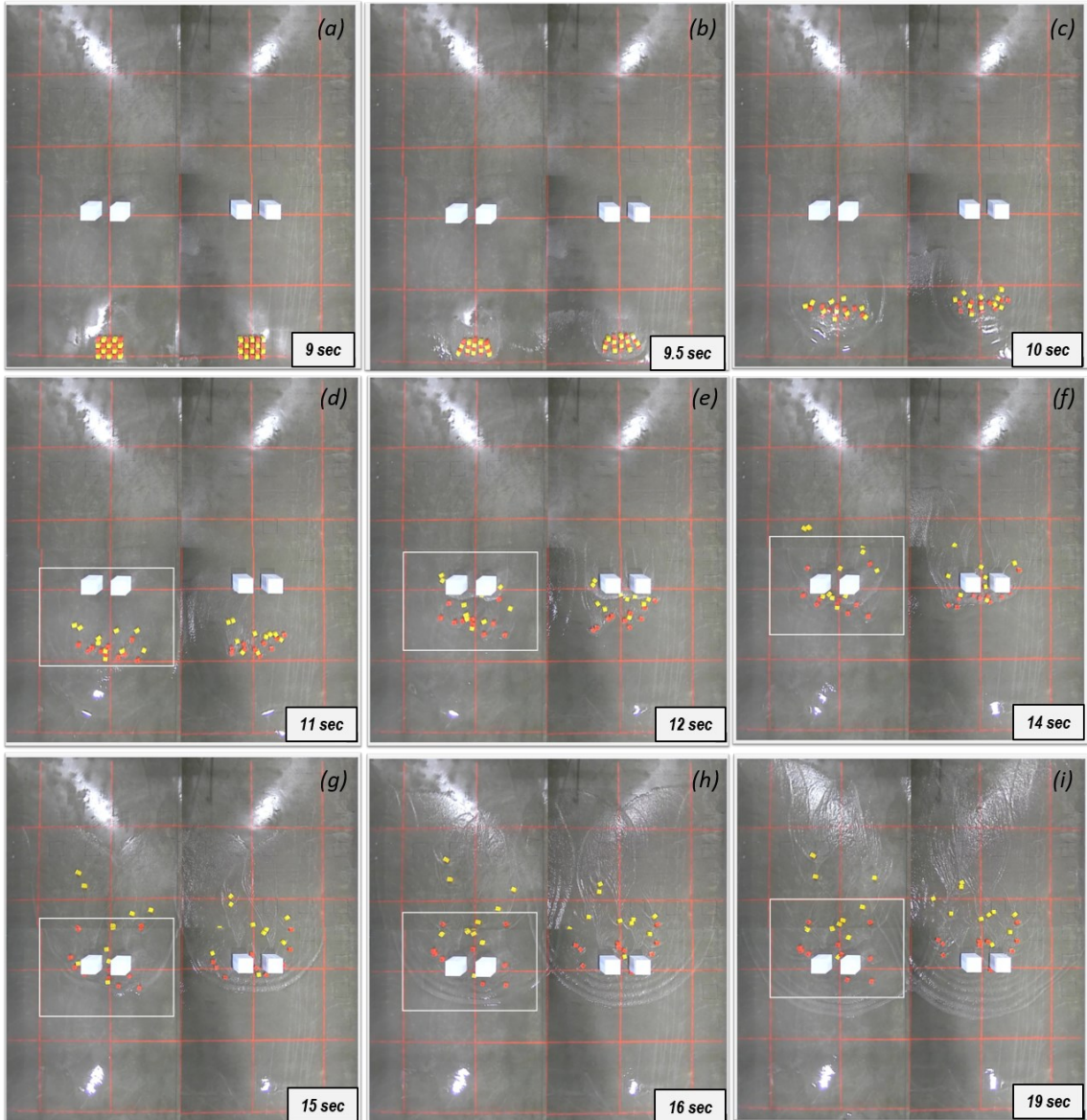
496

497 **5. Results of Debris Advection with Obstacles.**

498

499 Macro-roughness conditions provided by buildings or other structures strong enough to withstand the
500 hydrodynamic tsunami forces can significantly alter the flow dynamics (e.g., Park et al., 2013; Goseberg,
501 2013; Tomiczek et al., 2016; Qin et al., 2018; Winter et al., 2020), but the effects of those obstacles on the
502 debris advection are not understood yet clearly. In particular, the characteristics of flow fields and debris
503 transport are altered by the characteristics of obstacles, such as size, shape, position, and geometry, and
504 position of the obstacles. As described earlier in reference to Table 2, we tested debris advection with
505 obstacles in a relatively simple manner by the systematic addition of box-shaped obstacles at a fixed
506 distance landward of the debris field.

507 Analogous to Figure 7, Figure 14 shows a series of video images from Case 12 ($N_{obs} = 2$, $SG_g = 0.82$, C2
508 (Checker) configuration), and the white boxes indicate details shown in Figure 15. The leading edge of the
509 tsunami-like wave reaches the test sections at $t^* = 9$ s (Fig. 14a), and the debris initially forms radial
510 columns at $t^* = 9.5$ s (Fig. 14b). At $t^* = 10$ s, the columns are no longer visible, and the debris is still well-
511 mixed (Fig. 14c). By $t^* = 11$ s, sorting of debris is visible with the less dense debris (wood, yellow) leading
512 most of the denser debris (Fig. 14d). In the remaining frames, the debris can be seen to interact with the
513 obstacles with some of the debris flowing between and around the obstacles. Some of the debris elements
514 were seen to make contact with the obstacles. Starting at $t^* = 14$ s and continuing to $t^* = 19$ s, the leading
515 wave is partially reflected from the obstacles, and this reflection resulting in a raised water levels in front
516 of the obstacles affected the debris trajectories.



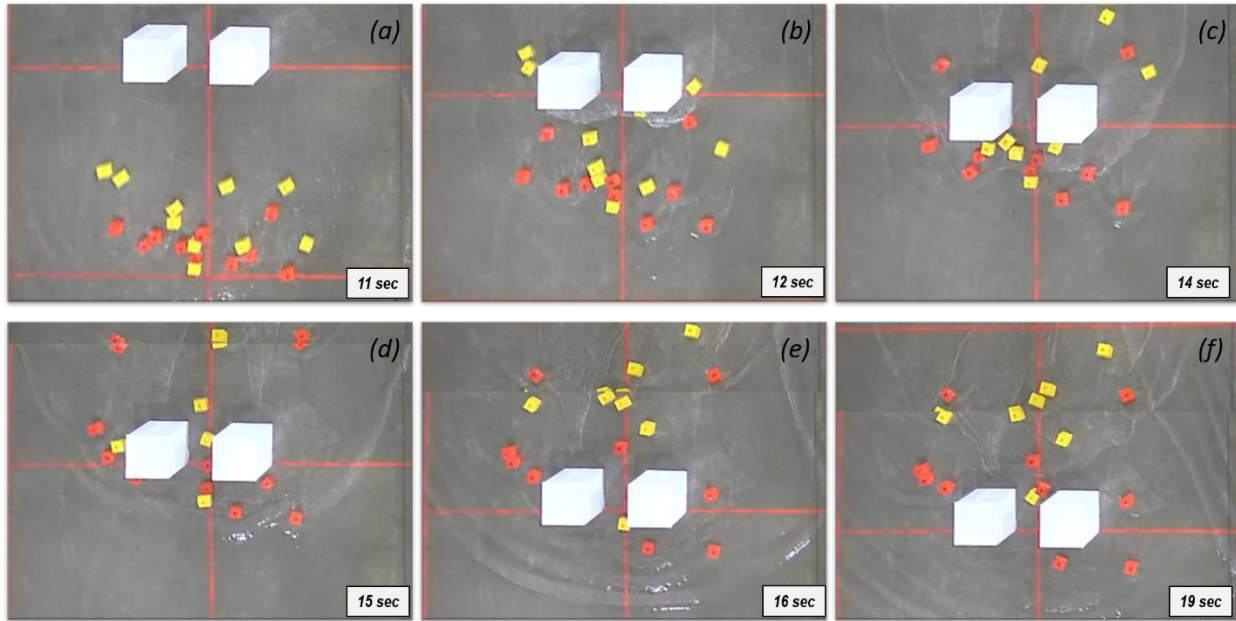
517

518 **Figure 14:** Snapshot of a series of the rectified image with $N_{obs} = 2$ (Case 12)

519

520 Figure 15 shows the series of detailed images from Figure 14 in the vicinity of the obstacles for $t^* = 11$,
 521 12, 14, 15, 16, and 19 s. Initially, the reflection developed at the front of an obstacle before the approach of
 522 debris (Fig 15 b). The reflection decelerated most of the debris motion nearby the obstacles and changed
 523 debris trajectories around obstacles, while some of the debris collided into the obstacles (Fig. 15c). Debris
 524 passed between obstacles at relatively low speed (Fig. 15d), and the debris accelerated as it passed between
 525 obstacles due to the wake developed behind of obstacles (Fig. 15e). Most of the debris elements that collided
 526 with the obstacles eventually passed between obstacles (Fig. 15f). Overall, an inspection of these figures
 527 shows interesting features described above, including the sorting of debris by density, the collision of debris

528 with the obstacles, the flow through and around obstacles, and the reflected wave developed from the
 529 obstacles that interfered with the debris.



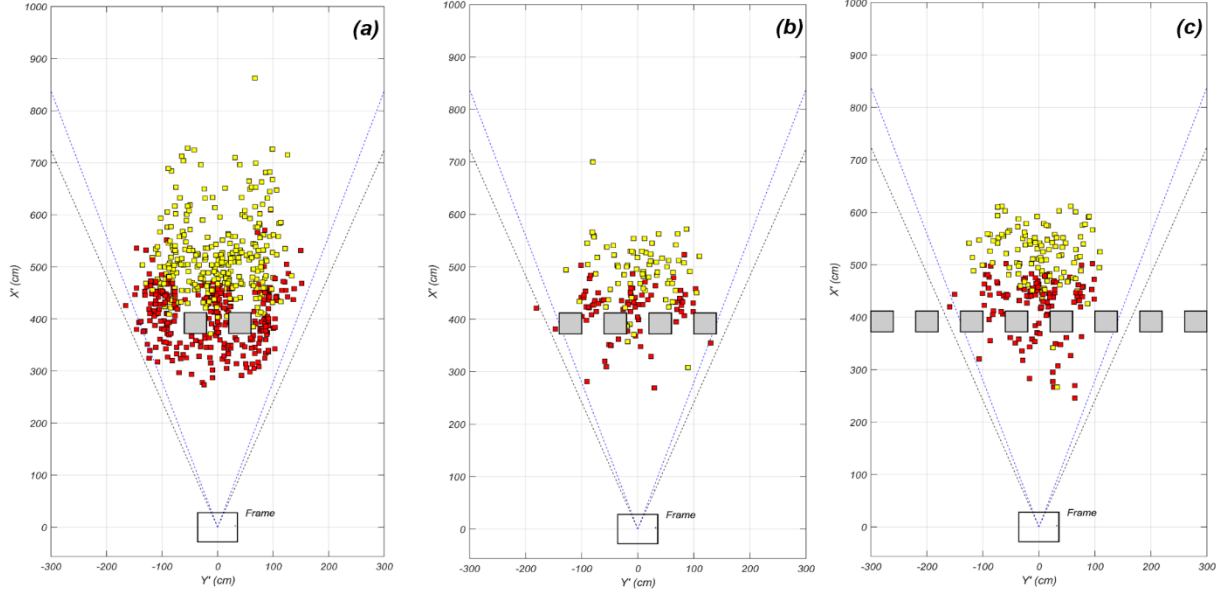
530

531 **Figure 15:** Series of detailed images near obstacles for Case 12 in Region A.

532

533 **5.1 Effects of obstacles on spreading angle and longitudinal distance**

534 Figure 16 shows the final locations of HDPE and wood debris for the three conditions of $N_{obs} = 2, 4, 8$.
 535 Figure 16a includes Case 11 to Case 14 with C2 (checker) and C3 (random) configurations with three SG_g
 536 conditions ($SG_g = 0.65, 0.82$, and 0.99). Figure 16b and 16c includes C2 (checker) and C3 (random)
 537 configurations with $SG_g = 0.82$ only. Similar to Figure 12 with no obstacles, Figure 16 shows that the less
 538 dense debris travels farther than the denser debris even with the presence of obstacles. The introduction of
 539 the two obstacles has a significant effect on the spreading angle and longitudinal distance relative to the no
 540 obstacle case (Figure 12). Somewhat surprisingly, however, the spreading angle and longitudinal distance
 541 are not significantly affected by the increasing number of obstacles, suggesting that there is a fairly narrow
 542 lateral limit to the effect that obstacles can have on debris transport.

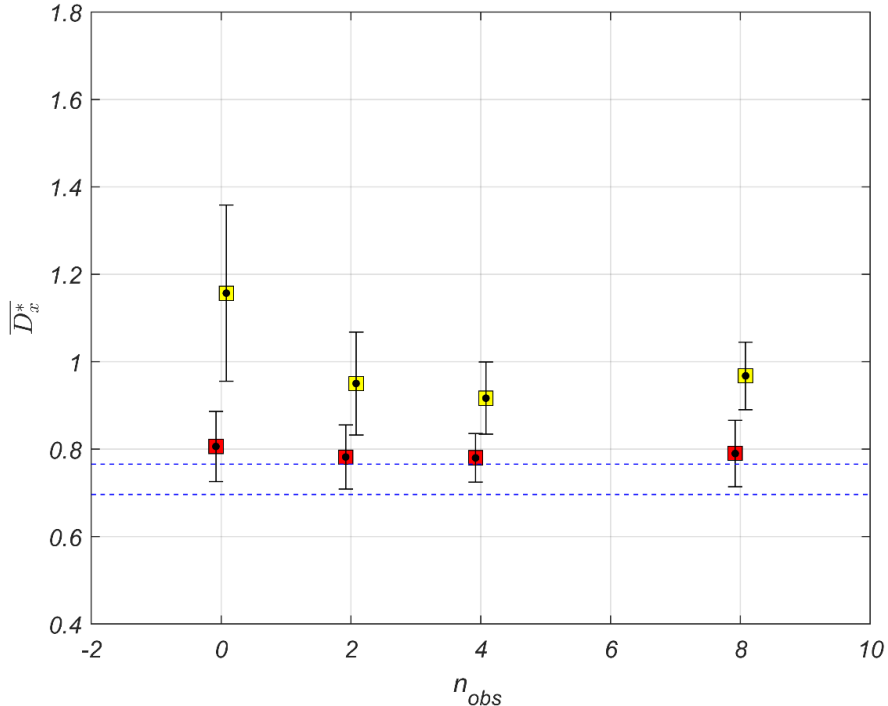


543

544 **Figure 16:** Final location for debris for three different obstacle cases: (a) Case 11 – 14 with $N_{obs} = 2$, (b)
 545 Case 15 - 16 with $N_{obs} = 4$, (c) Case 17 – 18 with $N_{obs} = 8$.

546

547 17 shows the mean normalized longitudinal distance \bar{D}_x^* and 95% confidence intervals for HDPE and
 548 wood debris for the cases with obstacles for $SG_g = 0.82$, including the case of no obstacles from Figure
 549 11. The two horizontal dashed lines indicate the location of the lower and upper edge of obstacles. Figure
 550 17 shows a significant decrease in \bar{D}_x^* for the less dense debris from $N_{obs} = 0$ to $N_{obs} = 2$ obstacles and then
 551 a constant \bar{D}_x^* as N_{obs} increased. The 95% confidence limit also decreases from $N_{obs} = 0$ to $N_{obs} = 2$
 552 obstacles. The dense debris, however, does not show a change in \bar{D}_x^* or 95% confidence limit as N_{obs}
 553 increases, even between the $N_{obs} = 0$ and $N_{obs} = 2$ cases.



554

555 **Figure 17:** Longitudinal distance \overline{D}_x^* with a different number of obstacles N_{obs} . Blue dashed lines indicate
 556 the lower and upper edge of obstacles.

557

558 To evaluate the potential change in spreading angle under different SG_g conditions with obstacles, we
 559 analyzed our results similar to that shown in Figure 13 and, for brevity, our results are summarized in Table
 560 4 which lists the spreading angle based on the 95% exceedance, q_{95} , for the left and right directions and the
 561 different SG_g conditions. The far-right column lists the mean absolute value for both directions and all SG_g
 562 conditions, $|q_{95}|_{mean}$. In general, the mean spreading angle of the higher density debris (HDPE) was larger
 563 than the lower density for both cases of with and without obstacles. The presence of obstacles increased
 564 the spreading angle for both debris types. These finding is contradictory to the previous observation, which
 565 showed lower spreading angles with the presence of obstacles to the downstream (Goseberg et al., 2016).
 566 The flow fields over obstacles and corresponding debris transportation are significantly altered by the
 567 geometry of obstacles (location, size, and gap) and debris size, number, and configurations). For example,
 568 the relative length scale of debris to obstacle (L/L_{obs}) in our study was 0.25, while it ranged about 0.5 to 2.0
 569 in Goseberg et al., 2016. Furthermore, the different tsunami inputs, flow fields (e.g., Froude number, and
 570 duration), different ratio of flow depth to draft, and different number of debris conditions will result in large
 571 variation in spreading angles.

572

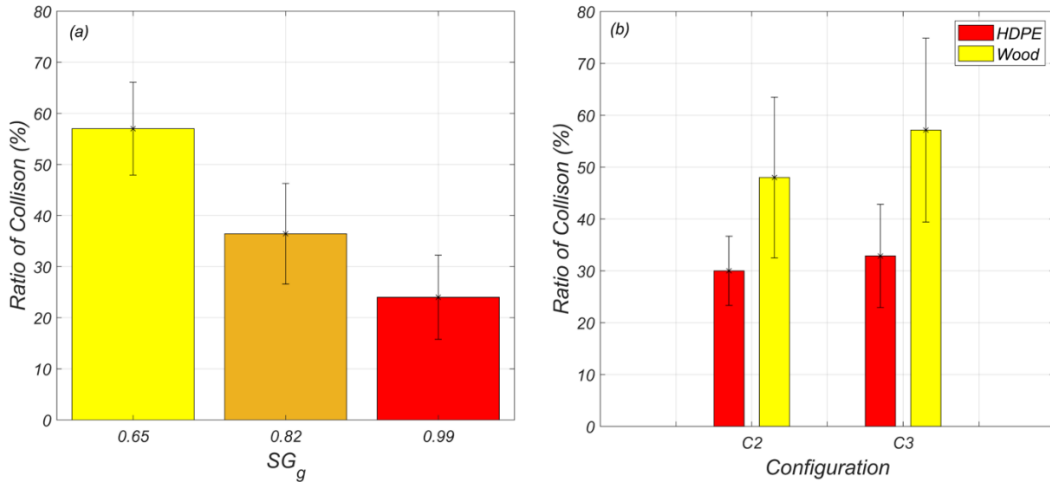
573 Table 4. Summary of spreading angles based on 95% exceedance (q_{95}) with and without obstacles.

Debris type	N_{obs}	Orientation	q_{95}					$ q_{95} _{mean}$
			$SG_g = 0.62$	0.73	0.82	0.91	0.99	
wood	0	Left	-6.8°	-8.9°	-8.7°	-12.5°	n/a	8.5°
		Right	9.0°	6.1°	7.1°	9.1°	n/a	8.5°
	2	Left	-10.7°	n/a	-12.8°	n/a	n/a	11.6°
		Right	11.1°		11.8°			11.6°
HDPE	0	Left	n/a	-12.0°	-13.1°	-14.6°	-18.2°	14.0°
		Right		11.1°	12.4°	15.7°	14.6°	14.0°
	2	Left	n/a	n/a	-15.7°	n/a	-20.9°	17.4°
		Right			15.7°		17.3°	17.4°

574

575 **5.2 Debris collision with obstacles**

576 The video images similar to those shown in Figure 14 were inspected to identify debris element collision
 577 with obstacles. Debris is classified as a collision case if debris is partially collided with obstacles and
 578 changed its moving direction. Figure 19a shows the total ratio of a collision of debris at three different SG_g
 579 conditions ($SG_g = 0.62$, 0.82, and 0.99) with standard deviations. Not all HDPE debris reached to obstacles
 580 and we excluded this debris to calculate the ratio of collision. There is a relatively high collision probability
 581 for $SG_g = 0.62$ (wood only) and a lower collision probability at $SG_g = 0.99$ (HDPE). This is perhaps counter-
 582 intuitive because it was initially thought that the higher density debris would have larger inertia and
 583 therefore would continue its trajectory into the obstacle. However, this was not the case, and it was observed
 584 that the wood debris element reaches the obstacle before the reflected wave was fully developed which may
 585 explain the observed differences. It might be a probability of grounding, depending on the individual draft
 586 of HDPE and wood debris. Therefore, we can expect that if we test the debris collision for different obstacle
 587 locations over different flow depth conditions, the collision probability trend would be different. This may
 588 also explain why the spreading angle of wood debris is relatively narrower than HDPE as shown in Table
 589 4.



590

591 **Figure 19:** Collision ratio according to HDPE rate and initial arrangement of debris
592

593 Figure 19b disaggregate the results of the $SG_g = 0.82$ cases by plotting the collision ratio separately for
594 HDPE and wood and also distinguish between the initial configurations, C2 (Checker) and C3 (Random).
595 Figure 19b shows that there is a clear distinction in the collision ratio, even when the debris types are mixed.
596 The initial configuration (Checker vs Random) does not seem to have had a strong effect.

597 **5.3 Debris velocity with and without obstacles**

598 As mentioned in the context of Figure 9, we use the optical measurements to estimate the mean u -velocity
599 (x-direction) of the leading-edge flow and individual debris elements at sections S1 to S6 identified in
600 Figure 9. Figure 20 shows the mean u -velocity of the leading-edge flow (blue), wood (black), and HDPE
601 (red) debris at the six sections (S1 to S6) at 100 cm intervals along the x-direction. The dashed and solid
602 lines indicate cases with obstacles and without obstacles, respectively. The centroid of the initial debris
603 field is at $X' = 0$, and the obstacles are centered at $X' = 397$ cm.

604 The mean velocity of leading-edge flow is nearly uniform for all sections from S1 to S6, increasing slightly
605 from S1 to S2, remaining constant from S2 to S4, and decreasing slightly from S4 to S6. The leading-edge
606 velocity is nearly the same for both cases, with and without obstacles, from S1 to S4 as expected and then
607 is lower in the lee of the obstacles.

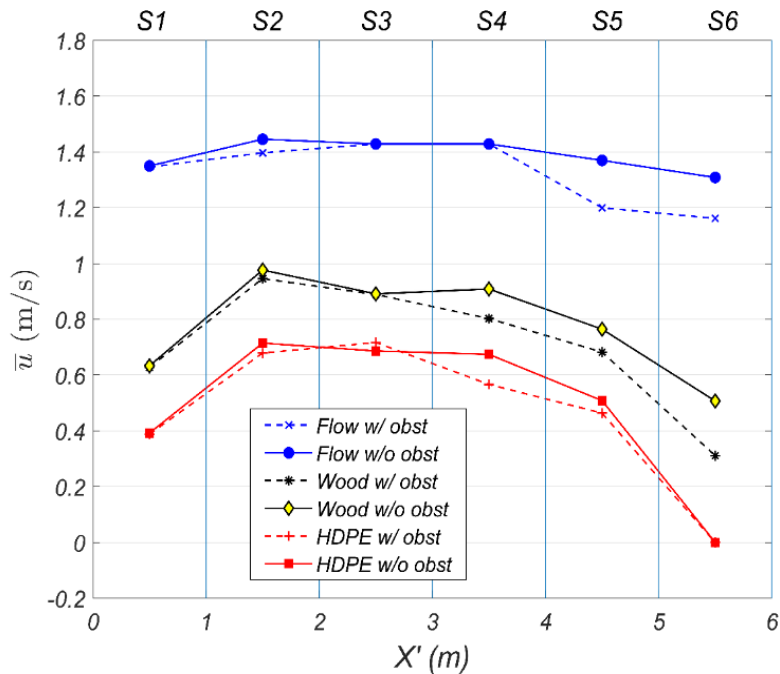
608 The velocity of the two debris types is lower than the leading edge velocity, with the wood debris reaching
609 70% of the leading edge velocity at S2 and the HDPE debris reaching 50% at S2. The velocity of the two
610 debris could not reach the leading edge velocity because of relatively short moving distance and lower flow
611 depth than the draft of each debris elements. To be specific, the maximum flow depth from S2 to S6 ranged
612 from approximately 4 cm (USWG_h1) to 1 cm (USWG_h7) from Fig. 4d, while the draft of HDPE and wood

613 is 5.03 and 3.30 cm. The velocity trends between the wood and HDPE are qualitatively similar from S1 to
 614 S3, and the HDPE reaches only about 70% of the wood debris velocity in these regions.

615 At S4, there is a clear decrease in the velocity of both debris' types just seaward of the obstacles relative
 616 to the cases without obstacles. This is a significant result because it shows that the presence of obstacles
 617 affects the velocity of the debris field. In some cases, individual debris elements were observed to reach
 618 very low velocities even though they did not directly collide with the obstacles. This decrease was often
 619 due to the reflected wave on the seaward side of the obstacle.

620 At S5 and S6 on the landward side of the obstacles, the wood debris velocity continues to be less than the
 621 velocity measured when no obstacles were present. On the other hand, the HDPE debris has only a very
 622 modest decrease in velocity at S5. At S6, the velocity is zero because the HDPE did not travel to this
 623 section as was shown in Figure 16.

624



625

626 **Figure 20:** Mean u-velocity of leading-edge and HDPE and wood debris with and without obstacles

627

628 **6. Discussion**

629

630 This study provides a unique experimental analysis of debris advected by a transient flow over a flat testbed
631 considering obstacles, representing an idealization of vehicles or shipping containers that would spread past
632 buildings during a tsunami or hurricane surge event. The current study evaluates the sensitivity of the final
633 longitudinal (inland) distance and spreading angle of debris transport due to the differences in debris density
634 and initial conditions. The results highlight that there is little effect of the initial conditions (i.e., the position
635 of higher or lower density elements within the initial field did not influence their final location or spreading
636 angle). However, there was a significant effect of density on the final location and spreading angle and the
637 collision probability of debris with obstacles. The specific ratio of relative flow depth to the draft of each
638 debris, and corresponding debris motion changes including grounding and wakes, should be quantified to
639 address the effects of density more clearly on debris transportation in the future.

640 Because these experiments were conducted at scale, we suggest a bit of caution in interpreting the results.
641 First, we observed about 10 s of inundation, which at 1:50 scale assuming Froude similitude would
642 correspond to 1.2 minutes in prototype conditions. This is much smaller than the typical tsunami inundation
643 time (10-30 min) observed for large tsunamis (e.g., Fritz et al., 2012). In any case, our observed differences
644 in the landward extent due to debris density would also be relevant over longer inundation durations.

645 A second idealization for these experiments involved the use of a flat slope for the test section. This slope
646 was utilized because the tests were conducted as part of a larger project for which the flat slope was designed
647 such that the water flowed over the flat section into a stilling basin on the landward. The flat slope
648 simplified the tests to some degree: the motion of the debris particles was laterally and in the onshore
649 direction only. The debris never went seaward. This is in contrast to debris movement observed in the
650 field where there can be seaward directed debris during the drawdown. Moreover, this is in contrast to the
651 laboratory observations of Rueben et al., 2015. Even though they had used a flat test section, their
652 experimental design did not allow for the overland flow to continue into a stilling basin. Instead, the flow
653 was reflected from the back wall and returned seaward, bringing the debris elements seaward, often to a
654 point more seaward than the initial starting location (see, for example, Figure 12b in Rueben et al., 2015).
655 Therefore, the importance of the return flow has not been considered in these tests. It is likely that
656 bathymetric and topographic features would further complicate the tsunami inundation and subsequent
657 overland flow and should be considered in future studies.

658 A third idealization involves the use of obstacles to represent the built environment. While the overall
659 length scale of the obstacles was chosen to correspond to buildings, the number and arrangement of

660 obstacles ($N_{obs} = 2, 4, 8$) and the spacing between the obstacles were chosen to simplify the testing and to
661 allow for comparison between Region A and B. In general, our tests showed that there is a limit to the
662 lateral influence of the obstacles. Figure 17, for example, show essentially no difference in the mean
663 longitudinal displacement $\overline{D_x^*}$ as the number of elements increases beyond $N_{obs} = 2$. However, this result
664 may be for this location only, and if the obstacles were placed at a more landward distance, it is possible
665 that $\overline{D_x^*}$ would be more sensitive to N_{obs} . Perhaps more importantly, the obstacles were only aligned laterally.
666 In other words, it would have been possible to use other arrangement obstacles (for example in staggered
667 rows and columns) that would have had a larger effect on the flow field and resulting debris trajectories
668 (Goseberg et al., 2016). Finally, the relative length scale of the debris elements to obstacles (1:4) was kept
669 constant using the uniform size of debris. The interaction of debris to obstacles and debris damming on
670 obstacles will be sensitive to the number and shape (or size) of debris too (Stolle et al, 2018a). Future studies
671 should consider how these geometry conditions of debris and obstacles affect the likelihood of impact and
672 damming or change in debris flow velocity.

673 We acknowledge that the work presented in this study represents a small subset of debris inundation under
674 idealized conditions. However, we anticipate that this work will be useful to guide the development and
675 verification of future numerical models for tsunami inundation with debris transportation that can be
676 potentially used to simulate a wider range of realistic conditions.

677 **7. Conclusion**

678

679 This paper presents an experimental study of tsunami-driven debris advection over the flat testbed. We
680 utilize two types of debris elements, which have the same shape but different materials (wood, HDPE) to
681 create debris of different densities. We considered variations in the grouping of debris (wood only, mixed
682 wood and HDPE, and HDPE only), parameterized by the mean specific gravity (SG_g), ranging from 0.65
683 (wood only) to 0.99 (HDPE only). We also considered the variation in starting conditions (e.g., mixed
684 debris with wood debris on the seaward side or landward side; uniform, checker, random starting patterns).
685 We introduced fixed obstacles landward of the initial debris field. *In-situ* instrumentation was used to
686 quantify the flow hydrodynamics (free surface, velocity), and cameras suspended from above were used to
687 quantify the debris trajectories. Tests were conducted with the same forcing condition (water level and
688 wavemaker displacement time history) and the same bathymetric conditions throughout the tests. In total,
689 46 tests were conducted. The main contributions and conclusions of this study are summarized below:

- 690 1. The less-dense debris group ($SG_g = 0.65$, wood) moved further and had less spread compared to a
691 more dense debris group ($SG_g = 0.99$, HDPE).
- 692 2. The mean longitudinal displacement \bar{D}_x^* of less dense debris decreased linearly as the amount of
693 more dense debris increased (Figure 11) in the debris group due to the interrupting influence by the
694 more dense debris during the advection. However, the mean longitudinal displacement \bar{D}_x^* of the
695 more dense debris was uniform. In summary, the more dense debris affected the mean longitudinal
696 displacement of the less dense debris, but the converse was not true.
- 697 3. The spreading angle of less dense debris increase slightly ($+3^\circ$) as the number of higher density
698 elements were added. The spreading angle of the more dense debris decreased (-9.7°) as the less
699 dense elements were added.
- 700 4. For groups with mixed debris, the initial configuration (e.g., wood debris on the seaward side or
701 landward side of the HDPE debris; uniform, checker, random starting patterns) had little effect on
702 the mean longitudinal displacement \bar{D}_x^* or spreading angle.
- 703 5. The cases with less dense debris (wood) only had a 30% higher probability of collision with the
704 obstacles compared to the cases with the more dense (HDPE) debris only. When the debris types
705 were mixed, the less dense debris has a lower probability of collision with the obstacles.
- 706 6. Overall, the reflected wave and interaction among different debris play a role in the probability of
707 collision. However, the density of each debris element was a dominant factor in determining the
708 collision probability.

709 7. The leading-edge flow velocity is spatially uniform ($\bar{u}=1.4 \text{ m/s}$) and greater than the less dense
710 debris ($\bar{u}=1 \text{ m/s}$) or more dense debris ($\bar{u}=0.7 \text{ m/s}$). The flow velocity of both debris types varied
711 spatially and was sensitive to the flow depth, a draft of debris, and the existence of obstacles.

712 In general, this paper highlights the importance of considering debris density in estimating the
713 longitudinal distance and spreading angle. These variables were less dependent on the initial
714 configuration of the debris field. Future studies should consider other aspects of the phenomena,
715 including a better understanding of the potential impact by debris on obstacles, the role of the return
716 flow in determining the debris trajectory, and investigations of the obstacles that more realistically
717 reflect urban shorelines subjected to strong overland flow.

718

719 **Acknowledgment**

720 The authors gratefully acknowledge the help of Sean Duncan, Adam Kean, Joaquin Moris Barra, Pedro
721 Lomonaco, and Tim Maddux to set up and performed this experiment. The authors thank the two
722 anonymous reviewers whose constructive comments significantly improved this manuscript. This material
723 in this study is based upon work partially supported by the National Science Foundation under awards
724 1519679 and 1661315. Any opinions, findings, and conclusions or recommendations expressed in this
725 material are those of the author and do not necessarily reflect the views of the National Science Foundation.

726

727 **7. References**

728

- 729 Aghl, P.P., Naito, C.J. and Riggs, H.R., (2015). Estimation of demands resulting from inelastic axial impact
 730 of steel debris. *Engineering Structures*, 82, pp.11-21.
- 731 AMERICAN SOCIETY OF CIVIL ENGINEERS. (2016). *Minimum design loads and associated criteria*
 732 *for buildings and other structures: ASCE/SEI 7-16*.
- 733 Bourgeois, J. and MacInnes, B., 2010. Tsunami boulder transport and other dramatic effects of the 15
 734 November 2006 central Kuril Islands tsunami on the island of Matua. *Zeitschrift für
 735 Geomorphologie, Supplementary Issues*, 54(3), pp.175-195.
- 736 Çelik, M., Ergun, Ö. and Keskinocak, P. (2015). The post-disaster debris clearance problem under
 737 incomplete information. *Operations Research*, 63(1), pp.65-85.
- 738 Chock, G.Y., 2016. Design for tsunami loads and effects in the ASCE 7-16 standard. *Journal of Structural
 739 Engineering*, 142(11), p.04016093.
- 740 Chock, G., Robertson, I., Kriebel, D., Francis, M. and Nistor, I. (2013). Tohoku, Japan, earthquake and
 741 tsunami of 2011: Performance of structures under tsunami loads. American Society of Civil
 742 Engineers.
- 743 Duncan S, DT Cox, A Barbosa, P Lomonaco, H Park, MS Alam, C Yu, Physical Modeling of Progressive
 744 Damage and Failure of Wood-Frame Coastal Residential Structures Due to Waves and Surge
 745 Forces, *Coastal Engineering*, (submitted, 7/2020).
- 746 Etienne, S., Buckley, M., Paris, R., Nandasena, A.K., Clark, K., Strotz, L., Chagué-Goff, C., Goff, J. and
 747 Richmond, B. (2011). The use of boulders for characterising past tsunamis: lessons from the 2004
 748 Indian Ocean and 2009 South Pacific tsunamis. *Earth-Science Reviews*, 107(1-2), pp.76-90.
- 749 FEMA, U. (2007). Public Assistance—Debris management guide. Dept. of Homeland Security
 750 Washington, DC.
- 751 Fritz, H.M., Phillips, D.A., Okayasu, A., Shimozono, T., Liu, H., Mohammed, F., Skanavis, V., Synolakis,
 752 C.E. and Takahashi, T. (2012). The 2011 Japan tsunami current velocity measurements from
 753 survivor videos at Kesennuma Bay using LiDAR. *Geophysical Research Letters*, 39(7).
- 754 Goseberg, N., 2013. Reduction of maximum tsunami run-up due to the interaction with beachfront
 755 development—application of single sinusoidal waves (2013). *Natural Hazards and Earth System
 756 Science* 13, Nr. 11.
- 757 Goseberg, N., Stolle, J., Nistor, I. and Shibayama, T. (2016). Experimental analysis of debris motion due
 758 the obstruction from fixed obstacles in tsunami-like flow conditions. *Coastal Engineering*, 118,
 759 pp.35-49.
- 760 Imamura, F., Goto, K. and Ohkubo, S., (2008). A numerical model for the transport of a boulder by
 761 tsunami. *Journal of Geophysical Research: Oceans*, 113(C1).
- 762 Lin, N. and Vanmarcke, E. (2008). Windborne debris risk assessment. *Probabilistic Engineering
 763 Mechanics*, 23(4), pp.523-530.
- 764 Martinez, E., Maamaatauaiahutapu, K. and Taillandier, V. (2009). Floating marine debris surface drift:
 765 convergence and accumulation toward the South Pacific subtropical gyre. *Marine Pollution
 766 Bulletin*, 58(9), pp.1347-1355.
- 767 Miller, J.A., Carlton, J.T., Chapman, J.W., Geller, J.B. and Ruiz, G.M. (2018). Transoceanic dispersal of
 768 the mussel *Mytilus galloprovincialis* on Japanese tsunami marine debris: An approach for
 769 evaluating rafting of a coastal species at sea. *Marine Pollution Bulletin*, 132, pp.60-69.

- 770 Murray, C.C., Maximenko, N. and Lippiatt, S. (2018). The influx of marine debris from the Great Japan
 771 Tsunami of 2011 to North American shorelines. *Marine pollution bulletin*, 132, pp.26-32.
- 772 Naito, C., Cercone, C., Riggs, H.R. and Cox, D. (2014). Procedure for site assessment of the potential for
 773 tsunami debris impact. *Journal of Waterway, Port, Coastal, and Ocean Engineering*, 140(2),
 774 pp.223-232.
- 775 Nistor, I., Goseberg, N. and Stolle, J. (2017a). Tsunami-driven debris motion and loads: A critical
 776 review. *Frontiers in Built Environment*, 3, p.2.
- 777 Nistor, I., Goseberg, N., Stolle, J., Mikami, T., Shibayama, T., Nakamura, R. and Matsuba, S. (2017b.)
 778 Experimental investigations of debris dynamics over a horizontal plane. *Journal of Waterway,
 779 Port, Coastal, and Ocean Engineering*, 143(3), p.04016022.
- 780 Kihara, N. and Kaida, H. (2020). Applicability of tracking simulations for probabilistic assessment of
 781 floating debris collision in tsunami inundation flow. *Coastal Engineering Journal*, 62(1), pp.69-
 782 84.
- 783 Ko, H.S., Cox, D.T., Riggs, H.R. and Naito, C.J. (2015). Hydraulic experiments on impact forces from
 784 tsunami-driven debris. *Journal of Waterway, Port, Coastal, and Ocean Engineering*, 141(3),
 785 pp.04014043.
- 786 Paris, R., Fournier, J., Poizot, E., Etienne, S., Morin, J., Lavigne, F. and Wassmer, P. (2010). Boulder and
 787 fine sediment transport and deposition by the 2004 tsunami in Lhok Nga (western Banda Aceh,
 788 Sumatra, Indonesia): a coupled offshore–onshore model. *Marine Geology*, 268(1-4), pp.43-54.
- 789 Park, H., Cox, D. T., Lynett, P. J., Wiebe, D. M., and Shin, S. (2013). Tsunami inundation modeling in
 790 constructed environments: A physical and numerical comparison of free-surface elevation,
 791 velocity, and momentum flux. *Coastal Engineering*, 79, 9-21.
- 792 Park H, Cox, D. T., Barbosa. A. R. (2018). Probabilistic Tsunami Hazard Assessment (PTHA) for
 793 Resilience Assessment of a Coastal Community, *Natural Hazards*, doi.org/10.1007/s11069-018-
 794 3460-3.
- 795 Park, H. and Cox, D.T. (2019). Effects of advection on predicting construction debris for vulnerability
 796 assessment under multi-hazard earthquake and tsunami. *Coastal Engineering*, 153, p.103541.
- 797 Prasetya, G., Black, K., de Lange, W., Borrero, J. and Healy, T. (2012). Debris dispersal modeling for the
 798 great Sumatra Tsunamis on Banda Aceh and surrounding waters. *Natural hazards*, 60(3), pp.1167-
 799 1188.
- 800 Qin, X., Motley, M.R. and Marafi, N.A. (2018). Three-dimensional modeling of tsunami forces on coastal
 801 communities. *Coastal Engineering*, 140, pp.43-59.
- 802 Riggs, H.R., Cox, D.T., Naito, C.J., Kobayashi, M.H., Piran Aghl, P., Ko, H.S. and Khowitar, E. (2014).
 803 Experimental and analytical study of water-driven debris impact forces on structures. *Journal of
 804 Offshore Mechanics and Arctic Engineering*, 136(4).
- 805 Rueben, M., Cox, D., Holman, R., Shin, S. and Stanley, J. (2015). Optical measurements of tsunami
 806 inundation and debris movement in a large-scale wave basin. *Journal of Waterway, Port, Coastal,
 807 and Ocean Engineering*, 141(1), p.04014029.
- 808 Shafiei, S., Melville, B.W., Shamseldin, A.Y., Beskhyroun, S. and Adams, K.N. (2016). Measurements of
 809 tsunami-borne debris impact on structures using an embedded accelerometer. *Journal of Hydraulic
 810 Research*, 54(4), pp.435-449.
- 811 Shekhar, K., Winter, A.O., Alam, M.S., Arduino, P., Miller, G.R., Motley, M.R., Eberhard, M.O., Barbosa,
 812 A.R., Lomonaco, P. and Cox, D.T. (2020). Conceptual Evaluation of Tsunami Debris Field

- 813 Damming and Impact Forces. *Journal of Waterway, Port, Coastal, and Ocean*
 814 *Engineering*, 146(6), p.04020033.
- 815 Stolle, J., Nistor, I., Goseberg, N., Mikami, T. and Shibayama, T. (2017). Entrainment and transport
 816 dynamics of shipping containers in extreme hydrodynamic conditions. *Coastal Engineering*
 817 *Journal*, 59(03), p.1750011.
- 818 Stolle, J., Takabatake, T., Nistor, I., Mikami, T., Nishizaki, S., Hamano, G., Ishii, H., Shibayama, T.,
 819 Goseberg, N. and Petriu, E. (2018a). Experimental investigation of debris damming loads under
 820 transient supercritical flow conditions. *Coastal Engineering*, 139, pp.16-31.
- 821 Stolle, J., Goseberg, N., Nistor, I. and Petriu, E. (2018b). Probabilistic investigation and risk assessment of
 822 debris transport in extreme hydrodynamic conditions. *Journal of Waterway, Port, Coastal, and*
 823 *Ocean Engineering*, 144(1), p.04017039.
- 824 Stolle, J., Nistor, I., Goseberg, N. and Petriu, E. (2020). Development of a Probabilistic Framework for
 825 Debris Transport and Hazard Assessment in Tsunami-Like Flow Conditions. *Journal of Waterway,*
 826 *Port, Coastal, and Ocean Engineering*, 146(5), p.04020026.
- 827 Sugawara, D., Goto, K. and Jaffe, B.E., (2014). Numerical models of tsunami sediment transport—Current
 828 understanding and future directions. *Marine Geology*, 352, pp.295-320.
- 829 Tachikawa, M. (1983). Trajectories of flat plates in uniform flow with application to wind-generated
 830 missiles. *Journal of Wind Engineering and Industrial Aerodynamics*, 14(1-3), pp.443-453.
- 831 Tomiczek, T., Wargula, A., Lomónaco, P., Goodwin, S., Cox, D., Kennedy, A. and Lynett, P. (2020).
 832 Physical model investigation of mid-scale mangrove effects on flow hydrodynamics and pressures
 833 and loads in the built environment. *Coastal Engineering*, 162, p.103791.
- 834 Tomiczek, T., Prasetyo, A., Mori, N., Yasuda, T. and Kennedy, A. (2016). Physical modelling of tsunami
 835 onshore propagation, peak pressures, and shielding effects in an urban building array. *Coastal*
 836 *Engineering*, 117, pp.97-112.
- 837 von Häfen, H., Stolle, J., Nistor, I. and Goseberg, N. (2021). Side-by-side entrainment and displacement of
 838 cuboids due to a tsunami-like wave. *Coastal Engineering*, 164, p.103819.
- 839 Winter, A. O., Alam, M. S., Shekhar, K., Motley, M. R., Eberhard, M. O., Barbosa, A. R., ... & Cox, D. T.
 840 (2020). Tsunami-Like Wave Forces on an Elevated Coastal Structure: Effects of Flow Shielding
 841 and Channeling. *Journal of Waterway, Port, Coastal, and Ocean Engineering*, 146(4), 04020021.
- 842 Xia, J., Falconer, R.A., Xiao, X. and Wang, Y. (2014). Criterion of vehicle stability in floodwaters based
 843 on theoretical and experimental studies. *Natural hazards*, 70(2), pp.1619-1630.
- 844 Yao, Y., Huang, Z., Lo, E.Y. and Shen, H.T. (2014). A preliminary laboratory study of motion of floating
 845 debris generated by solitary waves running up a beach. *Journal of Earthquake and Tsunami*, 8(03),
 846 p.1440006.
- 847 Yeh, H., Barbosa, A. and Mason, B.H. (2014). Tsunamis effects in man-made environment. *Encyclopedia*
 848 *of complexity and systems science*, pp.1-27.